A multidisciplinary approach to characterizing coastal alluvial aquifers to improve understanding of seawater intrusion and submarine groundwater discharge

Laura Martínez-Pérez, Linda Luquot, Jesús Carrera, Miguel Angel Marazuela, Tybaud Goyetche, María Pool, Andrea Palacios, Fabian Bellmunt, Juanjo Ledo, Nuria Ferrer, et al.

Journal of Hydrology 607 (2022) 127510

Contents lists available at ScienceDirect

Journal of Hydrology

journal homepage: www.elsevier.com/locate/jhydrol

Research papers

A multidisciplinary approach to characterizing coastal alluvial aquifers to improve understanding of seawater intrusion and submarine groundwater discharge

Laura Martínez-Pérez [a,b,c,*], Linda Luquot [d], Jesús Carrera [b,c], Miguel Angel Marazuela [a,b,c], Tybaud Goyetche [a,b,c], María Pool [b,c,e], Andrea Palacios [a,b,c], Fabian Bellmunt [f], Juanjo Ledo [f], Nuria Ferrer [a,b], Laura del Val [a,b], Philippe A. Pezard [d], Jordi García-Orellana [g,h], Marc Diego-Feliu [g], Valentí Rodellas [g], Maarten W. Saaltink [a,b], Enric Vázquez-Suñé [b,c], Albert Folch [a,b]

[a] Department of Civil and Environmental Engineering (DECA), Universitat Politècnica de Catalunya (UPC), Barcelona 08034, Spain
[b] Associated Unit: Hydrogeology Group (UPC-CSIC), Spain
[c] Geosciences Department, Institute of Environmental Assessment and Water Research (IDAEA), Severo Ochoa Excellence Center, Spanish Council for Scientific Research (CSIC), Barcelona 08034, Spain
[d] Géosciences Montpellier, Université Montpellier, CNRS, Montpellier 34095, France
[e] Amphos 21 Consulting S.L., Passeig Gracia i Faria 49, Barcelona 08017, Spain
[f] Institut de Recerca Geomodels, Universitat de Barcelona, Spain
[g] Institut de Ciència i Tecnologia Ambiental, Universitat Autònoma de Barcelona, Bellaterra, Spain
[h] Departament de Física, Universitat Autònoma de Barcelona, Bellaterra, Spain

ARTICLE INFO

This manuscript was handled by Corrado Corradini, Editor-in-Chief, with the assistance of Mohsen M. Sherif, Associate Editor

Keywords:
Coastal alluvial aquifer
Geological heterogeneity
Borehole geophysics
Conceptual model
Hydrogeochemistry

ABSTRACT

Coastal aquifers are affected by seawater intrusion (SWI), which causes their salinization, and yield submarine groundwater discharge (SGD), which feeds marine ecosystems. Characterizing groundwater dynamics in coastal aquifers is fundamental for understanding both processes and their interaction. In order to gain insights into SWI and SGD, we developed a 100 m-scale experimental field site located in a coastal alluvial aquifer at the mouth of an ephemeral stream on the Maresme coastline (Barcelona, Spain). Given the complexity of coastal aquifers and the dynamism of the processes occurring therein, understanding of the coupled processes can be achieved by combining methods and approaches across different hydrogeological disciplines. In this study, we conduct a detailed aquifer characterization based on the four pillars of hydrogeology: geology (lithological description and core samples analyses), geophysics (downhole and cross-hole measurements), hydraulics (pumping and tidal response tests) and hydrochemistry (major and minor elements, together with stable and Ra isotopes). Each discipline contributed to the characterization of the aquifer: (1) geological characterization revealed that the aquifer consists of fluvial sediments, organized in fining upwards sequences with alternating layers of gravel, sand and silt; (2) geophysics helped in identifying silt layers and their continuity, which play a segmenting role in the aquifer hydrodynamics; (3) hydraulics tests, specifically tidal response tests, evidenced that tidal loading, rather than hydraulic connection to the sea, drives the tidal response; and (4) hydrochemistry revealed a surprising high reactivity, as most ions reflect some reaction, beyond the expected cation exchange. The summary is that the aquifer, which initially looked like a homogeneous unconfined aquifer 22 m thick, effectively behaves as a multi-aquifer and reactive system with freshwater discharging beneath saltwater at several depths. The fact that thin silt layers caused such a significant impact opens new paths beyond this study both for coastal aquifer management (the possibility of transient pumping for freshwater resources) and marine ecology (expect diffuse groundwater discharge).

* Corresponding author at: Institute of Environmental Assessment and Water Research (IDAEA), CSIC, Barcelona 08034, Spain.
E-mail address: lauramartinez84@gmail.com (L. Martínez-Pérez).

https://doi.org/10.1016/j.jhydrol.2022.127510
Received 11 September 2021; Received in revised form 14 January 2022; Accepted 18 January 2022
Available online 25 January 2022

1. Introduction

Human settlements are rapidly increasing in coastal areas, representing a threat to groundwater resources. The rise in water demand, added to climate change, affects natural groundwater flow patterns and reduces its quality, making groundwater resources in coastal areas difficult to manage (Crossland et al., 2005). Consequently, the natural dynamic equilibrium between submarine groundwater discharge (SGD), and the reciprocal inland phenomena of seawater (SW) intrusion (SWI), is altered. This disequilibrium not only promotes the salinization of fresh groundwater resources, but also alters SGD and, thus, the nutrient supply to coastal ecosystems (Church, 1996; Moore et al, 1996; Younger, 1996; Kim and Swarzenski, 2010). The hydrological community has devoted significant research efforts to address the SWI problem (Werner et al., 2013; Michael et al., 2017) but only recently started to consider the SGD-SWI coupling (Zhou et al., 2018). Yet there is no clear methodology for addressing the management of either SWI or SGD, which probably reflects the complexity of both processes and their close interrelationship. Moreover, coastal systems are difficult to understand because of the many factors determining the interaction between freshwater (FW) and SW: temporal fluctuations of sea levels caused by tides; seasonal fluctuations of freshwater discharge; groundwater pumping; density dependent flow, water–rock interactions. Among extrinsic factors, the sedimentological and petrophysical complexity of coastal aquifers make their geochemistry equally complex. As a consequence, understanding the dynamic interaction of SGD-SWI requires a detailed characterization of both the small- and large-scale heterogeneities of the aquifer, as well as the fluxes and chemical components, by integrating various methodologies. In any event, such information is hard to obtain from coastal aquifers. Thus, much of the research conducted to date is based on theoretical and numerical frameworks (Pool and Carrera, 2011; Llopis-Albert and Pulido-Velazquez, 2014; Koussis et al., 2015; Bakker et al., 2017) or concentrated on specific aspects that influence coastal aquifer management, such as geology (Abarca, 2006; Zamrsky et al., 2020), geophysics (Goldman and Kafri, 2006; Falgàs, 2007; Duque et al., 2008), hydrodynamics (Guo et al., 2010; Chidichimo et al., 2015; Vallejos et al., 2015) and hydrochemistry (Ozler, 2003; Tamez-Meléndez et al., 2016). These approaches however constitute a paradigm of coastal aquifer analysis that may effectively hinder a comprehensive understanding of the interrelationship between SGD and SWI. In fact, as a dynamic process, some dissolution-precipitation reactions consistently occur at the freshwater-seawater interface (Andersen, 2005). In the long term, these reactions can induce changes in the structural properties of the aquifer, such as porosity and hydraulic conductivity (Plummer, 1975; Sanford and Konikow, 1989) and/or affect the composition of SGD (Moore and Joye, 2021). Although each specific discipline independently provides key information for the analytic conception of coastal aquifers, an integrative study based on the four main pillars of hydrogeology (geology, geophysics, hydraulics and hydrochemistry), is needed to fully characterize them.

The geology of sedimentary coastal aquifers is complex because conventional facies variability often increases due to the progradation-retrogradation deposits that develop after sea-level fluctuations associated with glaciations and eustatic movements. These kinds of sedimentary formations demand high-resolution data to unveil their overlapping structures (Gámez et al., 2009; Rovere et al., 2016). Core-data analyses can provide such information, essential for (1) understanding site sedimentology, (2) identifying minerals that may determine chemical reactions, and (3) characterizing and quantifying local hydraulic conductivity as well as, in general, small scale heterogeneities.

Geophysics, both in the form of downhole measurements and non-invasive surface geophysics, can help to identify different lithologies without sediment recovery, reducing coring and related costs and laboratory analyses. Specifically, total and spectral gamma ray (GR and SGR) logging are widely used in hydrogeological practice (Serra, 2008). Non-invasive geophysical images (electrical and electromagnetic, seismic, gravitational) provide two- and three-dimensional coverage beyond borehole geophysics at meter scale. These methods enable the visualization of geological structures and the definition of aquifer geometry, providing further information to classical geological surveys. Surface electrical and electromagnetic methods are sensitive to salinity contrasts. Hence, in coastal areas, electric-based methods have been used to define the extent of seawater intrusion. Unfortunately, loss of resolution at depth causes the seawater wedge to be poorly defined (Nguyen et al., 2009) which, in turn, is provided by borehole geophysics (Palacios et al., 2020).

Beyond aquifer structure, the dynamic exchange of fresh and marine waters is a key process in coastal aquifers. Characterizing their hydraulics is central to predicting and understanding flow paths and aquifer hydrodynamics. Classically, this assessment relies on the representation of piezometric maps to provide a snapshot of water levels in wells and pumping tests. Hydraulic characterization is the most common approach for quantitative evaluations because direct application of Darcy's law yields water fluxes. Unfortunately, heads measurements are hindered by difficulties associated to density variations and hydraulic testing is hindered by head fluctuations associated to sea level fluctuations (e.g., Carrera et al., 2009). Alternatively, tidal-based methods, which consist of observing the aquifer head response to tides and other sea level fluctuations (e.g., driven by wind or barometric pressure), provide a unique opportunity for the application of tidal response tests (Ferris, 1952; Carr and Van Der Kamp, 1969). These methods are easy to perform and provide information along the whole coast without disturbing the flow within the aquifer. Tidal response has instigated an extensive body of work for addressing the impact of heterogeneities, aquitard leakage and hydromechanical effects (HM) (Guomin and Chongxi, 1991; Li and Jiao, 2001; Slooten et al., 2010). Nevertheless, this approach is mainly academic and not yet widely implemented in hydrogeological practice, as an integrated study coupled to geological and structural properties is needed to evaluate the impact of heterogeneities on the tidal method.

Finally, hydrochemical investigations have been widely used to define the origin of dissolved compounds or groundwater composition. Hydrochemical characterization is especially relevant in coastal aquifers because the mixing of fresh and salt water drives numerous reactions, ranging from mineral dissolution or precipitation (Plummer, 1975; Sanford and Konikow, 1989) to ionic exchange, sulfate reduction and methanogenesis (Andersen, 2005). The study of hydrochemistry is also relevant for characterizing and quantifying SGD, which is now recognized as a major source of dissolved compounds (e.g. nutrients, metals) to the coastal sea (Moore, 2010; Beusen et al., 2013; Rodellas et al., 2015; Cho et al., 2018). The most widespread method for calculating SGD fluxes is based on the application of natural radioactive tracers present in coastal groundwater, mainly radium isotopes (^{226}Ra, ^{228}Ra, ^{224}Ra, ^{223}Ra) and radon (^{222}Rn) (Cook et al., 2018; Taniguchi et al., 2019, Garcia-Orellana et al., 2021). Groundwater is rich in these isotopes relative to seawater (Burnett et al., 2006). In addition, their different half-lives allow tracing processes that occur at different time scales and provide information on groundwater fluxes (Michael et al., 2011; Kiro et al., 2013; Rodellas et al., 2017; Tamborski et al., 2017; Debnath et al., 2019; Yi et al., 2019, Diego-Feliu et al., 2021). Given that ^{222}Rn is an inert gas and thus not influenced by the physicochemistry of coastal groundwater (e.g. pH, salinity, temperature) (Porcelli and Swarzenski, 2003), its distribution is mainly controlled by groundwater transit times and the uranium (and, specifically, ^{226}Ra) content in the aquifer solids (Dulaiova et al., 2008). Ra isotopes are influenced not only by the geological matrix, but also by the groundwater chemistry. It is well documented that Ra mobility has a strong dependence on the ionic strength of groundwater (Elsinger and Moore, 1980; Webster et al., 1995; Gonneea et al., 2008) but other factors (e.g. pH, grain size, reducing conditions) could also alter its concentration in groundwater (Szabo and Zapecza, 1991; Garcia-Orellana et al., 2021). The use of this natural radioactive tracer relies on an appropriate characterization of

tracer concentration in groundwater discharging to the coastal sea (SGD endmember), which is often the major source of uncertainty (Gonneea et al., 2008; Beck and Cochran, 2013; Duque et al., 2019). Consequently, hydrochemical information is not enough to quantify SGD and a full understanding of the aquifer geology, fluxes and spatial heterogeneity, is also required to perform an appropriate endmember characterization.

Characterization of coastal aquifers usually relies on more than one hydrogeologic approach, and it is frequent to find examples of the combination of at least two approaches, such as hydraulics and geophysics (Falgàs et al., 2011; Folch et al., 2020), or hydrochemistry and hydrodynamics (Xue et al., 2000; Li et al., 2009). However, the complexity of coastal aquifers may require greater integration of all the different aspects that determine the interaction between SGD and SWI in coastal aquifers. Moreover, taking small-scale features into consideration is needed for explaining observed behaviors at larger scales. As mentioned by Werner et al. (2013), there is still a lack of examples of real-world case studies implementing hierarchical methodologies focused on the characterization of heterogeneity and scale effect impact. In this study we apply various techniques based on the four pillars of hydrogeology under an integrative approach, with the objective of performing a detailed characterization of a coastal aquifer and the processes therein.

2. Methods

2.1. 2.1 Argentona experimental site

2.1.1. Experimental site hydrogeological context

The Argentona Stream is ephemeral and crosses the Catalan Coastal Range (CCR) towards the Mediterranean Sea (Fig. 1B). The CCR represents a tectonically elevated granitic horst that separates the Vallès depression from the coastal plain. The latter is part of an external depression developed mostly under the sea (IGME, 1976). Both structures are bound by two normal faults. One of these faults was responsible for the development of the Argentona Stream valley, which consists of Variscan granite and related plutonic rocks (granodiorites, tonalities, monzogranites, pegmatites, and dykes). The stream outlines a small Mediterranean catchment delimited at its northeastern part by a relief reaching up to 632 m and granitic outcrops ranging between 300 and 400 m of altitude, shaped by weathering and erosion (Riba, 1997; Cisteró and Camarós, 2014). Close to the shore, the Argentona Stream and its tributaries have developed heterogeneous Holocene alluvial deposits. Galofre (1969) estimated an average thickness of 20–30 m for the Holocene deposits. The composition ranges from granitic sands, gravels, and silt from the granitic saprolite, formed by weathering of plutonic and related metamorphic rocks (Bech, 1977; Bech et al., 1983).

The area where the Argentona Experimental site is located (Fig. 1A, B) was already identified as a promising site for the coupled study of SWI and SGD, as several studies identified both processes as being active in the area (Corominas and Custodio, 1981, Parra and Díaz, 2003, Cerdà-Domènech et al., 2017; Folch et al., 2020; Palacios et al., 2020).

2.1.2. Experimental site instrumentation

In order to monitor the aquifer, seventeen boreholes were drilled along a cross-shaped distribution (Fig. 1), determined from a preliminary surface electrical resistivity tomography survey (Ledo et al., 2016, *Internal communication*). We covered an experimental area of 1860 m^2, monitoring a 30 m length parallel to the coast and 62 m inland.

The experimental site is located on the right bank of the Argentona Stream. Its seawards end (Transect A-A') is located 40 m inland from the Sea. Towards the shoreline (Transect A-A'), 13 boreholes were drilled, 9 of them grouped in 3 nests (N1, N2, N3) and the other three as stand-

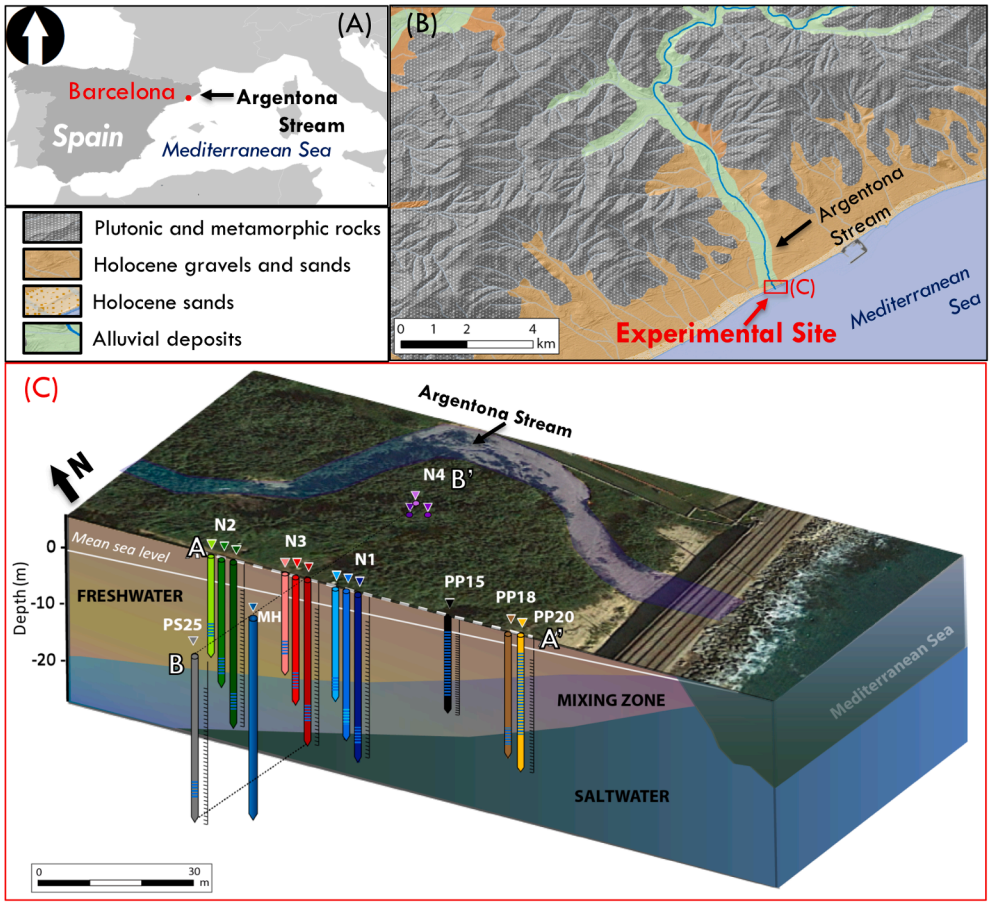

Fig. 1. Experimental site location and distribution of piezometers. (A) Context within the western Mediterranean basin. Source: Map Data (C) 2019 Inst. Geogr- Nacional (IGN) (B) Simplified geologic map of the Argentona Stream catchment. Source: Map Data(C) 2019 Inst. Geogr- Nacional (IGN), Inst Cartog-Geol-Cat (ICGC). (C) 3D block diagram of the experimental site. Cross-shaped distribution of piezometers following both sea-parallel and sea-perpendicular vectors, covering three depths (15, 20 and 25 m) grouped in nests, from inland to shore: N2, N3, N1 and closer to the streambed, N4. Single piezometer distribution (PS25, MH, PP15, PP20 and PP18) distributed both in the transverse (Transect A-A') and the sea-parallel branch (Transect B-B'). 25 m depth piezometers are equipped with permanent electrodes (black jagged lines). The slotted intervals are represented by blue stripes in each piezometer. Source: Imagery(C) 2019 Inst. Geogr- Nacional (IGN). (For interpretation of the references to colour in this figure legend, the reader is referred to the web version of this article.)

alone piezometers closer to the sea (PP15, PP18, PP20). The group of piezometers parallel to the shore (Transect B-B') was drilled to provide more detailed monitoring of the aquifer. It consists of two stand-alone piezometers (PS25 and MH), and a complementary nest (N4, 42 m near the streambed). Transect B-B' crosses Transect A-A' at the N3 nest (Fig. 1C).

Each nest consists of three piezometers: 15, 20, and 25 m deep (Fig. 1C), and have been labeled accordingly (Table 1). This configuration facilitates monitoring the shallow, intermediate, and deep zones of the aquifer. All the boreholes were cased with a PVC tube (8.9 cm internal diameter), with a blind end and a 2 m screened interval placed at different depths, except for two fully slotted piezometers (PP15 and PP20). The depths of the screened intervals coincide with the coarsest lens identified during drilling at each predetermined depth (see Table 1). MH borehole is a blind borehole filled with bentonite to couple electrical and thermal sensors to the formation.

Boreholes were equipped with different sensors. First, fiber-optic cable (BRUsens cable Temperature, Brugg Kabel AG, Switzerland) was installed in all boreholes in order to measure temperature with a "distributed temperature sensor" (DTS) as a continuous profile on the basis of the Raman effect (Folch et al., 2020). Second, in the deepest boreholes of each nest (N1-25, N2-25, N3-25, N4-25), and in PS25, PP15 and PP20, permanent instrumentation was installed to characterize spatial variations in subsurface resistivity using Cross-Hole Electrical Resistivity Tomography (CHERT). The equipment consists of 36 permanent electrodes attached to the PVC casing with different spacing depending on borehole length (Folch et al., 2020). This installation was used to obtain time-lapse CHERT images (Palacios et al., 2020). Third, a downhole electrical observatory called "Subsurface Monitoring Device" (SMD) was installed in the specific MH borehole drilled down to 28 m depth and equipped with a slotted PVC tube protected from fine particles using a sock. MH was filled with bentonite to study changes in aquifer electrical conductivity over time. An optical cable equipped with 14 Bragg networks was deployed along the electrical flute in MH to measure aquifer temperature with a precision greater than 0.01 °C.

2.2. Geological characterization at grain scale

Lithological characterization of the aquifer was based on the description of cores recovered from the deepest boreholes (see Table 1). The sediments were described and classified in terms of depositional sequences. To characterize the geochemistry, petrophysics, and mineralogy of the aquifer at cm-scale, 18 samples were extracted from borehole N1-25 (every 1.2 m, discarding the upper 3 m of soil) and analyzed by: (1) sieve analysis to determine the grain size distribution using a series of 7 progressively smaller mesh diameters, ranging from 5.0, 4.0, 2.0, 1.0, 0.5, 0.25, 0.1 to 0.063 mm; (2) multi-point BET (Brunauer-Emmet-Teller) gas adsorption method (Brunauer et al., 1938, Sinha, 2019) to measure the surface area of the sediment; (3) the Cu-Trien method (Stanjek and Künkel, 2018) to characterize total cation exchange capacity (CEC) and the amount of exchangeable cations (Na, K, Ca, Mg) to constrain ion-exchange reactions in the freshwater-saltwater interface; (4) X-Ray diffraction using a Bruker D8 Advance diffractometer to assess mineral content; (5) gamma spectrometry with a high-purity germanium detector (HPGe) to measure the content of U- and Th-decay products in sediments (including radium isotopes: ^{226}Ra and ^{228}Ra); (6) a Bartington MS2B sensor to evaluate magnetic minerals measuring magnetic susceptibility at two distinct frequencies −0.465 kHz (LF) or 4.65 kHz (HF)- and; (7) acid digestion (HNO_3, $HF/HClO_4$) to solubilize sediments and analyze them by Inductively Coupled Plasma-Atomic Emission Spectrometry (ICP-AES) using a Thermo Jarrel-Ash instrument to determine major and minor elements and Inductively Coupled Plasma-Mass Spectroscopy (ICP-MS) using an X-series II Thermo instrument to determine trace metals. The same analytical procedures were later used for hydrochemical analysis (see Section 2.5).

2.3. Geophysical characterization

Different borehole geophysical measurements were used to characterize petrophysical properties (magnetic susceptibility, formation electrical conductivity and K, U Th content) at borehole scale (Table 1). Gamma Ray (GR) profiles were recorded using a standard gamma ray probe in 8 boreholes to first characterize the distribution of K-rich sediments with depth. Measurements were performed by deploying a probe at a controlled speed inside the PVC piezometers and recording variations in the natural gamma radiation using a NaI scillintation detector. The locations of areas with high gamma ray counts per second (CPS) marked the presence of fine-grained layers that will serve to establish the stratigraphic correlation between boreholes (Cripps and McCann, 2000). Spectral Gamma Ray (SGR) was also recorded in all the experimental site boreholes using the Antares Spectral Natural Gamma Probe Datensysteme GmbH, equipped with a BGO (bismuth germanate) scintillation crystal. This spectral sensor informs about the presence of K, U and Th in the formation along each borehole with a data point every 5 cm and a spatial resolution of 50 cm. The spectral approach based on 256 energy windows facilitates the determination of the relative contribution of the three elements to the SGR signal (Hesselbo, 1996) thus enabling the identification of zones with high Th and U content, potential sources of natural tracers (radium isotopes), and K-rich layers with higher clay content (Schlumberger, 2009). The Geovista EM51

Table 1
Characteristics of the different types of boreholes and relation of downhole geophysical data. Being EC_b: Bulk electrical conductivity of the formation, MS: magnetic susceptibility, SGR: spectral gamma-ray, GR: total gamma-ray, ERT: electrodes along the borehole, SMD: Subsurface Monitoring Device. All boreholes are equipped with fiber-optic (FO) cable.

Borehole type	Name	Distance from the sea (m)	Piezometer depth (m)	Slotted interval depth (m)	Core recovery	Geophysics
Nest N1	N1-15	63	17	13–15	No	EC_b, MS, SGR
	N1-20	60	22	18–20	No	EC_b, MS, SGR
	N1-25	62	25	21–23	Yes	ERT, GR, SGR
Nest N2	N2-15	98	14	10–12	No	EC_b, MS, SGR
	N2-20	100	19	15–17	No	EC_b, MS, SGR
	N2-25	98	26	20–22	Yes	ERT, GR, SGR
Nest N3	N3-15	80	14	10–12	No	EC_b, MS, SGR
	N3-20	80	20	16–18	No	EC_b, MS, SGR
	N3-25	78	25	18–20	Yes	ERT, GR, SGR
Nest N4	N4-15	82	17	10–12	No	EC_b, MS, SGR
	N4-20	81	19	14–16	No	EC_b, MS, SGR
	N4-25	83	25	18–20	Yes	ERT, GR, SGR
Single	PP15	52	15	2–13	No	ERT, GR, SGR
	PP20	40	20	3–18	No	ERT, GR, SGR
	PP18	40	18	13–15	No	EC_b, MS, SGR
	PS25	83	25	18–20	No	ERT, GR, SGR
	MH	83	28		Yes	EC_b, MS, SGR, SMD

electromagnetic induction probe was deployed in the shallower and intermediate piezometers with no permanent geophysical instrumentation (N1-20, N1-15, N3-15, N3-20, N4-20, N4-15, N2-20, N2-15) (Table 1). This sensor records simultaneous induction electrical conductivity and the magnetic susceptibility profiles of the formation. The electrical conductivity of the formation (EC_b) is controlled by porosity, pore connectivity, surface electrical conduction within pores, and, especially, pore water salinity and temperature, (Archie, 1942; Waxman and Smits, 1968) and can be obtained through the following equation: $EC_b = EC_w/F + C_s$,where EC_w is the electrical conductivity of water, F the formation factor, and C_s a surface conduction term (Waxman and Smits,1968). On the other hand, magnetic susceptibility profiles (MS) provided data related to the solid phase of the formation in response to an applied magnetic field, thus enabling the localization of fine-grained horizons, possibly rich in magnetic minerals and/or oxide alteration (Dearing, 1994).

Permanent borehole instrumentation enabled imaging 2D transects of apparent resistivity using a Syscal-Pro multi-channel. Cross-Hole Electrical Resistivity Tomography (CHERT) acquisitions were performed in the deepest boreholes aligned perpendicularly to the sea and two stand-alone (or single) piezometers (in an inland-seaward trajectory: N2-25, N3-25, N1-25, PP15 and PP20) (Palacios et al., 2020).

2.4. Hydraulic parameters characterization: from grain to site scale

Hydraulic characterization entails measuring heads and hydraulic parameters to assess groundwater flow. As the actual hydraulic conductivity (K) [$L{\cdot}T^{-1}$] is difficult to measure in the field, transmissivity (T) [$L^2{\cdot}T^{-1}$] is more frequently derived from hydraulic tests, such as pumping tests. Nevertheless, small scale K can be obtained from grain size distributions. In this study we applied different methods to quantify the hydraulic properties of the aquifer at different scales.

2.4.1. Grain scale analysis

At the cm-scale, K was determined based on the grain size distributions using two different empirical relationships: $K_H = C_H{\cdot}(d_{10})^2$ (Hazen, 1911) and $K_S = C_S{\cdot}d_{50}^j$ (Shepherd, 1989). The first relationship is frequently applied to sands as it relies on the effective grain size (d_{10}). The dimensionless C_H coefficient depends on sorting and ranges around 100 for d_{10} in mm and K_H in cm/s. The second relationship is meant for a broader range of sediment types (depends on the median grain size d_{50}), as reflected by the C_S coefficient and dimensionless exponent j depending on the type of deposits (Fetter, 2018). We later averaged the small-scale values for hydraulic conductivity (K) of the samples placed at the same depth as the piezometers' slotted intervals from the cluster N1, in order to evaluate the transmissivity at borehole scale using $T = K{\cdot}b$ (being b the thickness of the considered layer). For the shallowest interval (N1-15), we assigned 1 m thickness for samples n1-8 and n1-12, which are located at the extreme limit of the slotted interval (see Table 3 for sample depth and Table 1 for slotted interval depth). For the intermediate slotted interval (N1-20), we calculated transmissivity using small-scale hydraulic conductivities for samples n1-13 and n1-14, while for the last interval (N1-25), we only have the small-scale hydraulic conductivities of sediments corresponding to its upper part (represented by sample n1-15, Table 3).

2.4.2. Borehole scale analysis

During borehole clean-up, after drilling and the installation of the PVC piezometers, 17 single-borehole pumping tests of one-hour duration were carried out in each piezometer. These tests provided local transmissivity values for the sedimentary units of each slotted interval in the vicinity of the piezometer. Pumping tests were performed using an electrical suction pump and pressure transducers (Schlumberger, USA; Solinst, Canada) to monitor drawdown evolution in the pumping well. Pumping rates ranged between 0.2 and 1 $L{\cdot}s^{-1}$, depending on the expected transmissivity for each borehole. Transmissivity was estimated through the empirical relation between transmissivity and specific well capacity ($T \approx 1{,}2{\cdot}(Q{\cdot}s^{-1})$) (Mace, 2001).

2.4.3. Site scale analysis

At site-scale, hydraulic diffusivity (D_H) was derived from tidal response analysis. Changes in heads were recorded from conductivity-temperature-depth sensors (CTDs) in boreholes every 15 min and compared to sea level oscillations. First, a filtering step was performed to remove the effects of wind, atmospheric pressure, and waves. Subsequently, non-tidal noise was removed and a spectral analysis was applied to locate tidal signal harmonics in the sea and in the boreholes, together with its main components (see equations in Supplementary Material).

2.5. Hydrochemical sampling: borehole scale analysis

A total of 18 water samples were collected after a relatively dry period (January 22th, 2016) from the site boreholes (except MH and PP18), the sea and an upstream borehole. We consider this sampling campaign as the hydrochemical baseline for the lower part of the Argentona aquifer.

Groundwater samples were taken at different aquifer depths (depending on the sampled piezometer; see Table 1). Three times the volume of water contained inside the PVC tube of each piezometer was purged (between 40 and 110 L) before sampling, to ensure the collection of aquifer water. A centrifugal pump was used to extract groundwater at a low flow rate of 0.5 $L{\cdot}min^{-1}$ to minimize mobilization. The pump was placed in the middle of the slotted intervals to reduce the impact of mixing between waters within the borehole. A flow cell was installed at the outlet of the sampling tube to avoid the interaction of groundwater and air. The cell was equipped with a multi-parameter probe to measure in-situ temperature, dissolved oxygen (DO), pH, Eh, and water electrical conductivity (EC_w).

Groundwater samples selected for cation analyses were filtered in the field using 0.2 μm syringe filters before refrigeration and storage. To avoid mineral precipitation, 0.15 mL of ultrapure HNO_3 was added. Major ion and trace elements were analyzed by the ICP-AES and ICP-MS equipment mentioned in Section 2.2. Phosphates (PO_4, and total P) were determined by spectrophotometry while the rest of the nutrients (NH_4, NO_2, and NO_3) and anions (Cl^-, SO_4^{2-}, Br^-, F^-) were analyzed by ion chromatography. On sample aliquots, we analyzed stable isotopes ($\delta^{18}O$ and δ D) to identify the different sources of groundwater (Gat and Gonfiantini, 1981; Clark and Fritz, 2013) by comparing values with the local meteoric water line (LMWL) defined by (Neal et al., 1992). $\delta\ ^{18}O$ composition was determined by equilibrium with a mixture of 0.3% CO_2 gas with He using a mass spectrometer (MAT-253 Thermofisher) and δ D was analyzed using a pyrolizer coupled continuous flow mass spectrometer (TC/EA-IRMS Delta Plus XP Thermofisher).

The activity of the radioactive tracers (Ra isotopes and ^{222}Rn) was measured for specific groundwater samples taken at the 11 points located on the line perpendicular to the sea. 60 L of groundwater were extracted from each piezometer and filtered through MnO_2 fibers at a controlled flow rate (<1 $L{\cdot}min^{-1}$) to extract Ra isotopes from the solution (Moore, 1976). The short-lived Ra isotopes (^{224}Ra and ^{223}Ra) contained in the fibers were analyzed using the Radium Delayed Coincidence Counter (RaDeCC) (Moore and Arnold, 1996) and quantified following the recommendations made by Diego-Feliu et al. (2020). After measuring these isotopes, the fibers were ashed, grounded and transferred to counting vials and aged for a minimum of 3 weeks to quantify the long-lived isotopes (^{226}Ra and ^{228}Ra) by gamma spectrometry using a high-purity well-type Ge detector. For ^{222}Rn analysis, water samples were collected in 250 mL air-tight bottles, ensuring minimum water–air interaction. ^{222}Rn samples were analyzed using the radon-in-air monitor RAD7 coupled to a gas extraction accessory bottle (Durridge Inc.) (Burnett et al., 2001).

3. Results

3.1. Geological and geochemical characterization of the aquifer

This section describes the aquifer structure at different scales and the complete geochemical characterization using the cores extracted from the deep wells (N1-25, N2-25, N3-25, and N4-25).

The textural description highlighted four main sediment types according to the Folk and Ward (1957) classification: gravelly sand, sandy gravel, gravelly muddy sand and slightly gravelly sand. The extracted cores are a combination of variable proportions of these textural groups, whose composition varies from metamorphic and quarzitic to granitic. Gravels often contain different portions of lithic fragments. Sediments present a sandy to silty matrix and are organized in layers of variable thickness. The general mineralogical composition of cores is similar for all the extracted samples. It consists, on average, of 56% of both sodium and potassium feldspar (albite and microcline), 20% quartz, 18% mica (illite) and 5% amphibole (Fe-rich Mg-Hornblende). Detailed mineral composition can be found in Table 2.

Textural description of the sediment recovered from the deepest wells leads to the lithological cross-section of Fig. 2. The lateral continuity is observed and the same depositional sequences are identified in the different boreholes. It is relevant to point that the continuity of the layers at 7.5–8.4 and 17 m depths was not noticed initially. However, tidal response tests and CHERT suggested a semiconfined behavior. After re-analyzing the cores and GR profiles, we concluded that these layers were indeed continuous. The sediments are arranged in 7 fining-upwards depositional sequences: 3 coarse-grain dominated sequences (I-III, Fig. 2) that resemble fining-upwards beds in the upper part of the aquifer (from 0 to 12 m depth), and 4 other sequences of equal type (IV-VII, Fig. 2), but with finer-grain size in the lower part (from 13 to 22 m depth).

Moreover, we found minor layers of silt located at the top of sequences II and V (at 7.5–8.4 and 17 m) and another more continuous one at the top of sequence IV (at 12 m depth). The granulometric analysis performed on 11 samples extracted from the N1-25 core, identified a fine-grained layer at 7.5 m depth (sample n1-4) (Fig. 3A). Despite this, the average grain size of the analyzed sediments is medium to very coarse sand (0.4 mm to 2.0 mm) with a tendency to be finer with depth (see d_{10} evolution in Fig. 3A). This decrease in grain size was also observed during sequence definition.

The BET surface area (Fig. 3B) and CEC (Fig. 3C) present low and constant values for almost the whole of the aquifer profile. In sequences I-VI (Fig. 2), BET ranges between 0.5 and 1.2 $m^2 \cdot g^{-1}$, and the CEC average value is 1.6 $cmol \cdot kg^{-1}$, except between 7.5 and 8.4 m depth, where BET increases up to 3.2 $m^2 \cdot g^{-1}$ (samples n1-4 and n1-5, Fig. 3B). As expected, a direct relation is observed between grain size and BET surface area, with a higher surface for a smaller grain size. At depth, BET surface area, CEC and total exchangeable cations (Na, Mg, K, Ca) present their maximum value below sequence VII (around 21 m, sample n1-15, (Fig. 3B, C and D respectively). Below this depth, both the total CEC and the exchangeable Na decrease again in the weathered granite (samples n1-16, n1-17, n1-18) to reach an average value of 6.1 $cmol \cdot kg^{-1}$, which is higher than the values measured at shallower depths (sequences I-VI). Magnetic susceptibility, measured in discrete samples (Fig. 3E), presents maximum values at the top of sequences III, IV and VII. Activities of ^{226}Ra are almost constant and lower than ^{228}Ra. Nevertheless, a major increase in ^{226}Ra is measured also at the top of Sequence III (in sample n1-5 at 8.4 m, Fig. 3F). Another increase in ^{226}Ra but also in ^{228}Ra is located in the bottom part of the aquifer (sample n1-16) in the weathered granite. ^{228}Ra shows higher variability in depth than ^{226}Ra, with slightly higher values for samples n1-1, n1-4, n1-12 and n1-16, representing silty materials in most locations.

Fig. 4 displays major and minor elements (expressed in weight percent). Prominent peaks of MnO, Fe_2O_3, TiO_2 and MgO can be distinguished in sequences III, V and VII (samples n1-5, n1-12 and n1-14 at 8.4 m, 17.5 m, and at 19.5 m depth respectively).

In general terms, in the upper part of the aquifer (sequences I-IV), we observe the same trend for all the elements, whereas in the lower part (sequences V-VII), Na_2O (Fig. 4A) and CaO (Fig. 4B) follow a similar pattern, opposite to Fe_2O_3, TiO_2 and MgO. MnO is also slightly different (Fig. 4G), with higher concentrations at the top of sequences III and IV (samples n1-5 and n1-9).

Regarding trace elements, Ba is the most abundant and with a typical granitic concentration of between 420 and 840 $\mu g \cdot g^{-1}$ (Mielke, 1979).

Table 3
Hydraulic conductivity (K) obtained from grain size analyses.

Sequence	Sample	Depth (m)	K_S($m \cdot d^{-1}$)	K_H($m \cdot d^{-1}$)
I	n1-1	4.5	950	450
	n1-2	5.7	440	500
	n1-3	6.4	7970	3040
II	n1-4	7.5	10	~1
	n1-5	8.4	2100	90
III	n1-6	10	470	70
	n1-8	11.3	50	4
V	n1-12	17.5	2170	110
	n1-13	18	100	10
VI	n1-14	19.5	10	4
	n1-15	20.9	60	20

Table 2
Mineral composition in % obtained through X-Ray diffraction (XRD) of the samples extracted from the different sequences of borehole N1-25. (Traces of lizardite were also found in samples N1-10 and n1-17 and clinochlore in sample n1-12).

Sequence	Sample	Depth (m)	Slotted interval correspondence	Quartz	Microcline	Albite	Illite	Fe-rich Mg-hornblende
I	N1- 1	4.5		27	21	42	10	–
	N1- 2	5.7		19	27	31	23	–
	N1- 3	6.4		31	16	38	16	–
II	N1- 4	7.5		14	34	31	17	4
	N1- 5	8.4		28	14	37	17	4
III	N1- 6	10.0		18	24	31	21	7
	N1- 7	11.0		26	27	44	3	–
	N1- 8	11.3		14	19	37	24	7
IV	N1- 9	12.0		30	24	38	8	–
	N1- 10	13.2	N1-15	28	24	21	26	–
	N1- 11	14.4	N1-15	27	22	46	5	–
V	N1- 12	17.5		19	27	38	13	3
	N1- 13	18.0	N1-20	20	29	30	16	6
VI	N1- 14	19.5	N1-20	18	32	35	14	–
Undefined	N1- 15	20.9		18	23	26	33	–
	N1-16	22.0		–	–	–	–	–
–	N1- 17	22.5	N1-25	15	10	36	38	–
	N1- 18	24.0		37	24	33	6	–

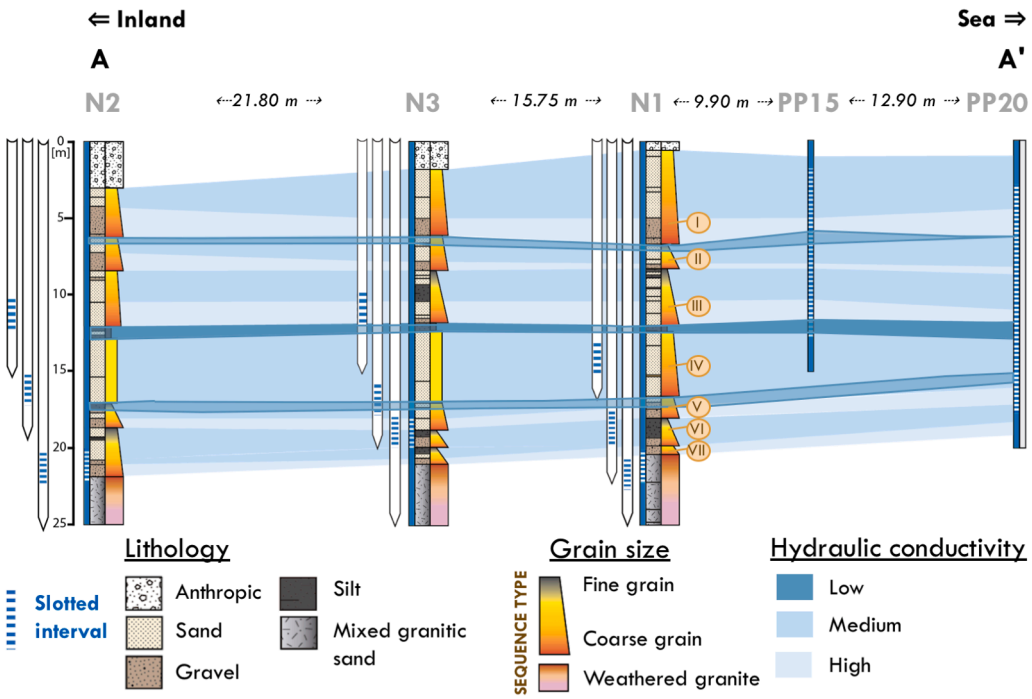

Fig. 2. Lithostratigraphic correlation between 25 m depth boreholes drilled perpendicular to the sea with core recovery (see localization of Transect A-A' in Fig. 1) and localization of the differentiated sequences in borehole N1-25. Continuous qualitative hydraulic conductivity fields, based on grain sizes identified during core descriptions, are indicated in blue scale. (For interpretation of the references to colour in this figure legend, the reader is referred to the web version of this article.)

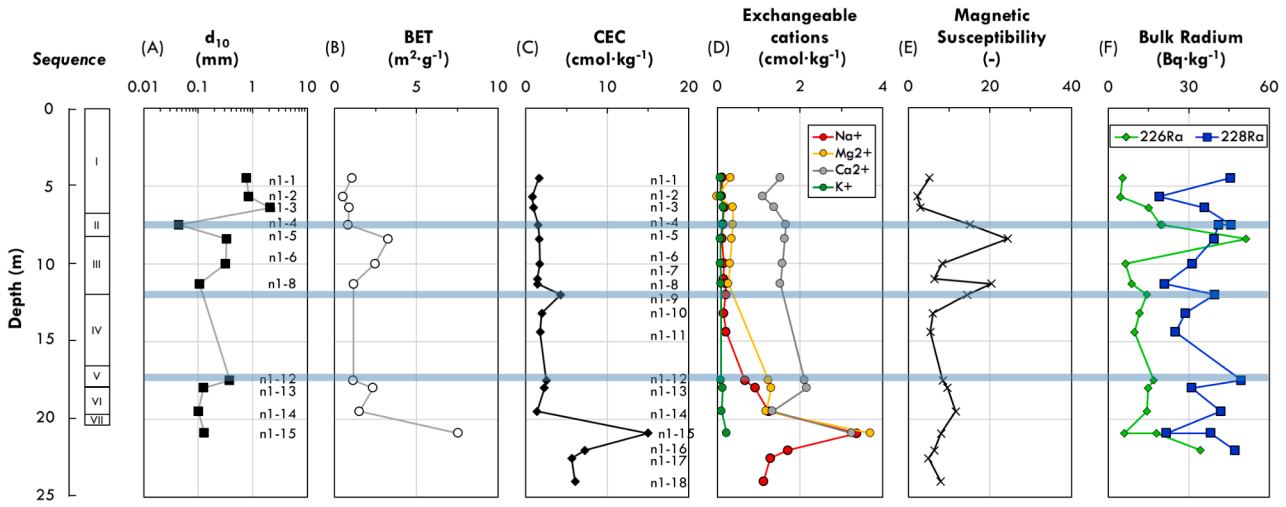

Fig. 3. Grain and geochemical analysis of core samples extracted from the different sequences of borehole N1-25. (A) Effective grain size d_{10} derived from sediment analysis, (B) Brunauer-Emmet-Teller (BET) surface area, (C) total cation exchange capacity (CEC) (D) exchangeable cations, (E) magnetic susceptibility (MS), (F) bulk radium concentrations according to depth. The trace of the silty zones is marked in blue. (For interpretation of the references to colour in this figure legend, the reader is referred to the web version of this article.)

The highest Ba concentrations are measured in samples n1-4, n1-5, n1-9 and n1-14 (Table S1, Supplementary Material). Th and U concentrations, which are the chain parents of the measured long-lived Ra isotopes, are almost constant with depth, except at the bottom of sequence I (sample n1-3) and in sequence V (sample n1-12) where slightly higher Th and U concentrations are measured. At the bottom of Sequence I, we found the coarsest sample and the only one with peaks in Co, Ni, Pb, Bi, W and Sn concentrations (sample n1-3).

3.2. Geophysical assessment

Downhole geophysical logs performed on each nest are plotted together to facilitate comparison among both boreholes and techniques (see Fig. 5). SGR data (Fig. 5 and Fig. S1 Supplementary Material) from the different boreholes are similar. Together, they confirm the continuity of the layers mentioned in the geological characterization.

In general, an increase in SGR (CPS) is observed bellow 20 m in all boreholes (Fig. 5). On the contrary, downhole MS data remains somewhat constant with depth (Fig. 5), except for the high values recorded at the top of sequence III (about 8 m depth). EC_b generally increases with depth. However, a sharp increase of more than 600 mS·m^{-1} is observed at 15 m depth in all logs (Fig. 5). Further down, borehole MH shows a decrease below 18 m with a minimum at around 20 m depth before increasing again. Relatively high EC_b values can also be observed in the

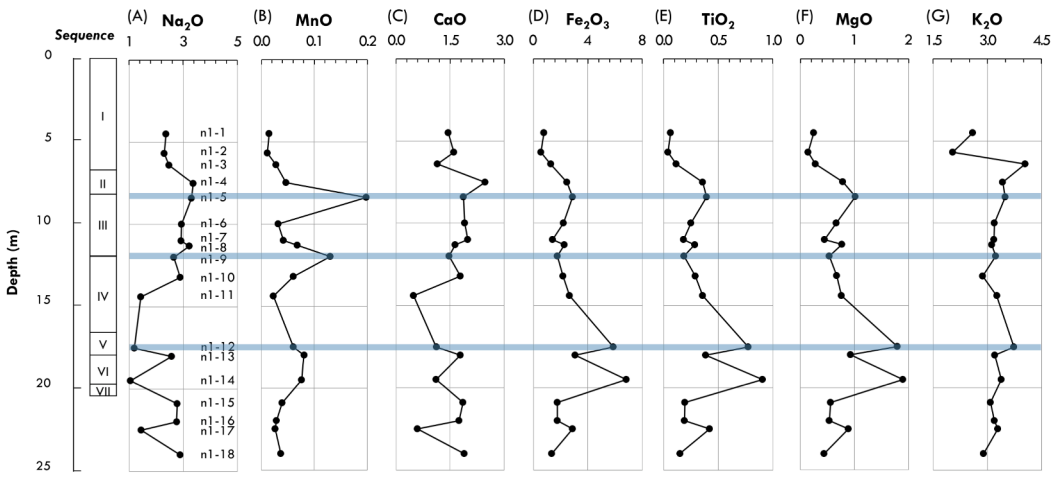

Fig. 4. Major and minor element concentration (expressed as oxide weight %) obtained from sediment samples taken from borehole N1-25 with respect to depth. The trace of the silty zones is marked in blue. (For interpretation of the references to colour in this figure legend, the reader is referred to the web version of this article.)

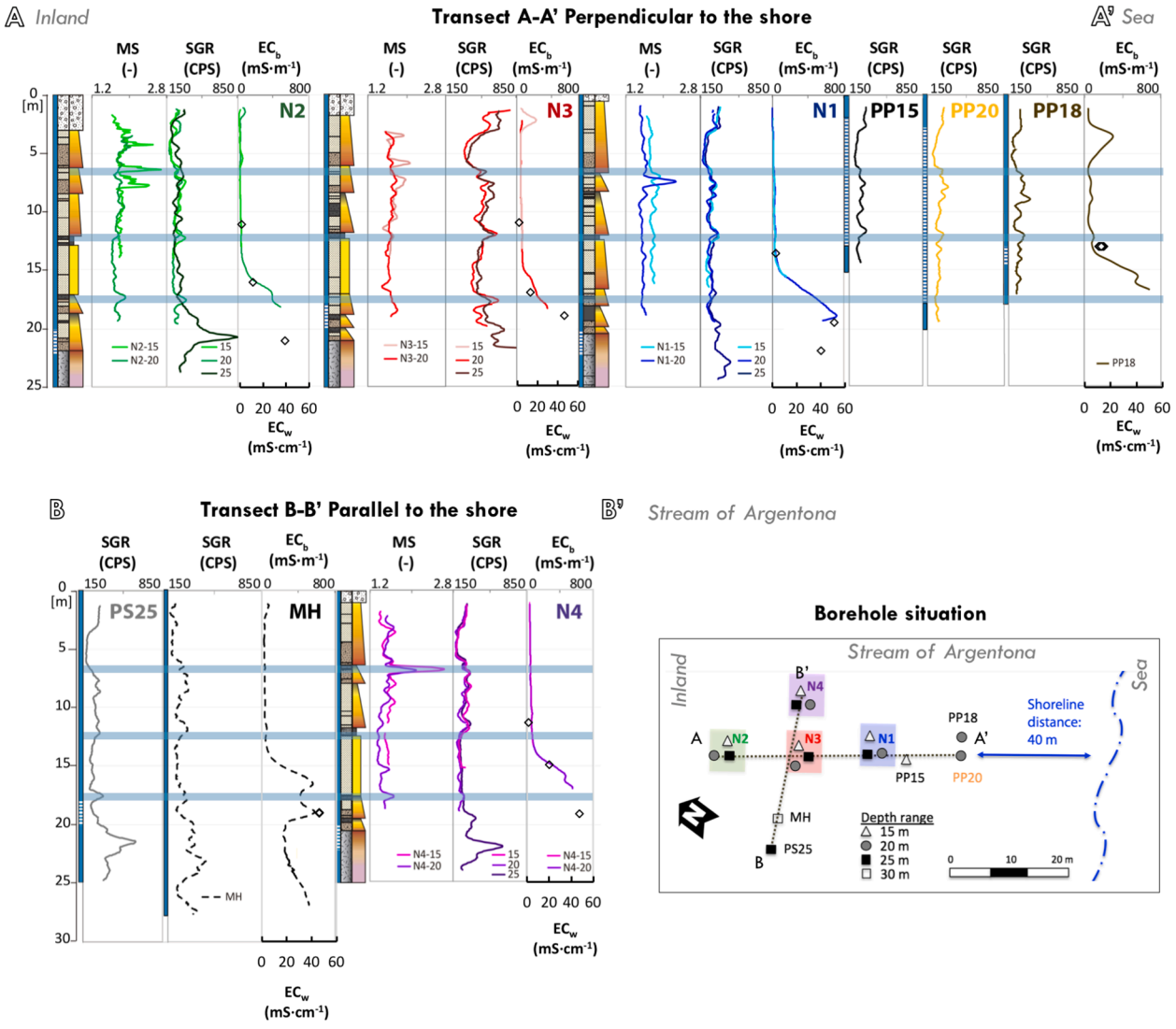

Fig. 5. Integration and correlation of downhole measurements (MS: Magnetic susceptibility; SGR: Spectral Natural Gamma Ray; EC_b: Bulk electrical conductivity of the formation) and stratigraphic column of the deepest boreholes (25 m). The trace of the three main silt layers within the Experimental Site has been added in blue horizontal lines. Electrical conductivity measurements of groundwater samples (EC_w) are shown as open circles. (For interpretation of the references to colour in this figure legend, the reader is referred to the web version of this article.)

upper portion of some boreholes (N2-25, N3-15, PP18, and MH).

The Th/K ratio can be derived directly from SGR data (Fig. S1B, Supplementary Material) and it is related to clay mineralogy, which is consistent with the fine materials described in the stratigraphic description. The Th/K ratio displays peaks at the top of sequences III, IV and V (7.5–8.4, 12 and 17.5–18 m depth). Also, high Th/K values are reached at around 21 m. Approaching the sea, the magnitude of these Th/K maximums decreases from a value of 13.4 at the inland extreme of the experimental site (N2-25) to 6.7 at the well closest to the sea (PP20) (Fig. S1B, Supplementary Material).

3.3. Hydraulic characterization

The grain size distribution of sediment samples extracted along N1-25 enabled the calculation of small-scale hydraulic conductivities (K). Results are shown in Table 3 described in Section 2.4.1. Values obtained using the Shepherd equation (K_S) tend to be an order of magnitude larger than those of Hazen (K_H), but they correlate quite well (correlation coefficient of 0.9 in log scale). As a general trend, both K values tend to decrease with depth although they are quite variable, which is to be expected in these types of deposits, where fine-grained layers alternate with coarse-grained layers. Illustratively, three layers of high hydraulic conductivity are identified at 6.4, 8.4 and 17.5 m depth. Also, low K values are obtained at three different depths (7.5, 11.3 and 19.5 m, in Table 3). This distribution of K is consistent with the stratigraphic description defined in the section on aquifer geology.

Short pumping tests performed in each piezometer provided borehole scale transmissivities ($T_{borehole}$ in Table S2, Supplementary Material). They are considered representative of the meter scale and the volume of the aquifer surrounding the borehole. Short pumping tests localized zones of low transmissivity in the deepest boreholes located in the weathered granite (Table 1). Borehole scale transmissivities are considered representative of the area surrounding the well (m-scale), whatever the sedimentary unit. PP15 and PP20, fully screened boreholes, show $T_{borehole}$ values in the range of the other boreholes located in the same sedimentary sequence or relatively higher. As the 2 m screened boreholes of this unit are located in the coarsest lens identified during drilling, $T_{borehole}$ values obtained in PP15 and PP20 could be representative of the highly permeable layers located close to the pumping depth (at 10 and 15 m respectively).

We compared the equivalent transmissivities ($T_{Hazen\ lab}$ and $T_{Shepherd\ lab}$) obtained from small-scale hydraulic conductivities (cm-scale) with short hydraulic pumping tests performed in the corresponding slotted intervals (m-scale) of N1 ($T_{borehole}$ in Fig. 6). As expected, both methodologies show different values as they represent different aquifer matrix scales and volume. However, transmissivities obtained at both scales present the same trend with depth. If we compare N1 with the other nests, it is possible to observe a similar trend, with transmissivity increasing slightly in the shallower part of the aquifer before decreasing at depth (Table S2, Supplementary Material).

At the site scale, tidal analysis revealed that fluctuations observed in boreholes reflect sea level fluctuations. The spectral analysis (Fig. S2A, Supplementary Material) shows the same tidal harmonics in the aquifer and in the sea. Tidal fluctuations seem to be dominated by semi-diurnal (M2) and diurnal (K1 and O2) components. These components have already been described by Arabelos et al. (2011) and Toro y Llaca et al. (1994) for the western part of the Mediterranean Sea. Fig. S2B (Supplementary Material) shows that the time lag is short for all piezometers, but especially short for intermediate depth wells. A short lag might suggest a good connectivity to the sea, but would be inconsistent with their depth (hydraulic connection would have to be across the upper layers). This, together with the low value of the lag compared to the amplitude damping, led us to conclude that the observed response is largely hydromechanical (HM) (Goyetche et al, *in press*). The fact that the shallowest boreholes located in the sedimentary materials show different lag than intermediate boreholes located in the same geological formation, indicate that the aquifer acts as a multilevel aquifer.

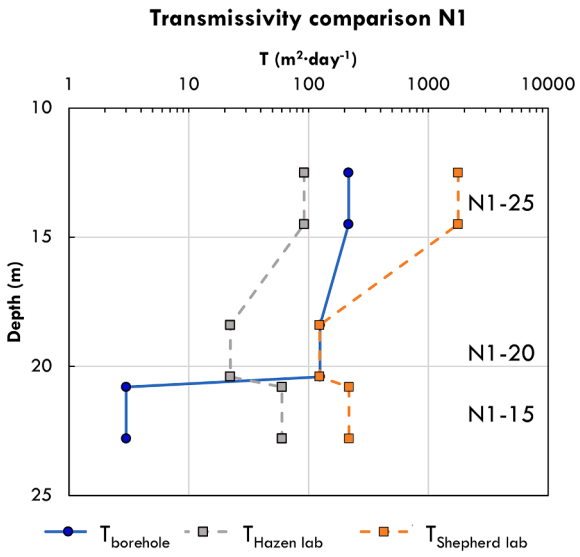

Fig. 6. Comparison of transmissivities ($T_{Hazen\ lab}$ in grey and $T_{Shepherd\ lab}$ in orange) obtained from grain size distribution and short hydraulic tests performed on nest N1 ($T_{borehole}$ in blue, see values in Table S2). Equivalent transmissivities ($T_{Hazen\ lab}$ and $T_{Shepherd\ lab}$) were obtained taking into consideration the values obtained from K_{Hazen} and $K_{Shepherd}$ (see Table 3) at each slotted interval (for N1-15: samples n1-8 and n1-12, for N1-20: sample n1-13, and for N1-25: sample n1-15). (For interpretation of the references to colour in this figure legend, the reader is referred to the web version of this article.)

3.4. Hydrochemical and isotopic assessment

EC_w measured from groundwater samples tends to increase with depth, as expected (Fig. 7C). However, the increase is non-monotonic. For the closest piezometers to the coastline (N1 and the fully penetrating piezometer, PP20), we recorded higher EC_w at intermediate depths (between 15 and 19 m) than at depth (N1-25). Dissolved oxygen (DO, Fig. 7B) is low (around 1 $mg{\cdot}L^{-1}$) and tends to zero with depth. pH is low in the aquifer, much lower than the freshwater and seawater end-members (7.8 and 8.1, respectively) and tends to decrease with depth, showing an increasing acidification in the lower part of the aquifer (Fig. 7C). Eh values are higher at shallow and intermediate sampling points and then decrease at depth (Fig. 7D). Nitrate concentration (Fig. 7E) tends to decrease with depth (affected by SWI) and is often accompanied by an increase in boron in some deep boreholes (Fig. 7F). The other chemical elements (Fe and Mn) tend to increase with depth (Fig. 7G-H). Recorded concentrations of major ions can be found in Table S3 (Supplementary Material). All these observations suggest that the site is extremely active from a hydrochemical point of view.

Groundwater type is defined using the Piper diagram (see Fig. S3 in Supplementary Material). Three groundwater types have been described and evolved from Ca-HCO_3 for the freshest shallow boreholes, to Ca-Cl for the intermediate part of nests N2, N3, and N4 and NaCl for the deepest boreholes.

Fig. 8 plots various ions versus Cl concentrations. If there was only mixing between the fresh- and sea-water end-members without chemical reactions (conservative mixing), all points would lay on a straight mixing line between the two end-members. Points above the line indicate enrichment and points below indicate depletion by chemical reactions (or mixing with a third end-member). Only stable isotopes behave conservatively, which confirms the high reactivity of the site. Deviations from the conservative mixing line are maxima in the deepest boreholes, slotted between 19 and 22 m depth. In particular, the observed Ca enrichment (Fig. 8A) can be attributed to mineral dissolution and/or ionic exchange with Na. However, alkalinity measurements

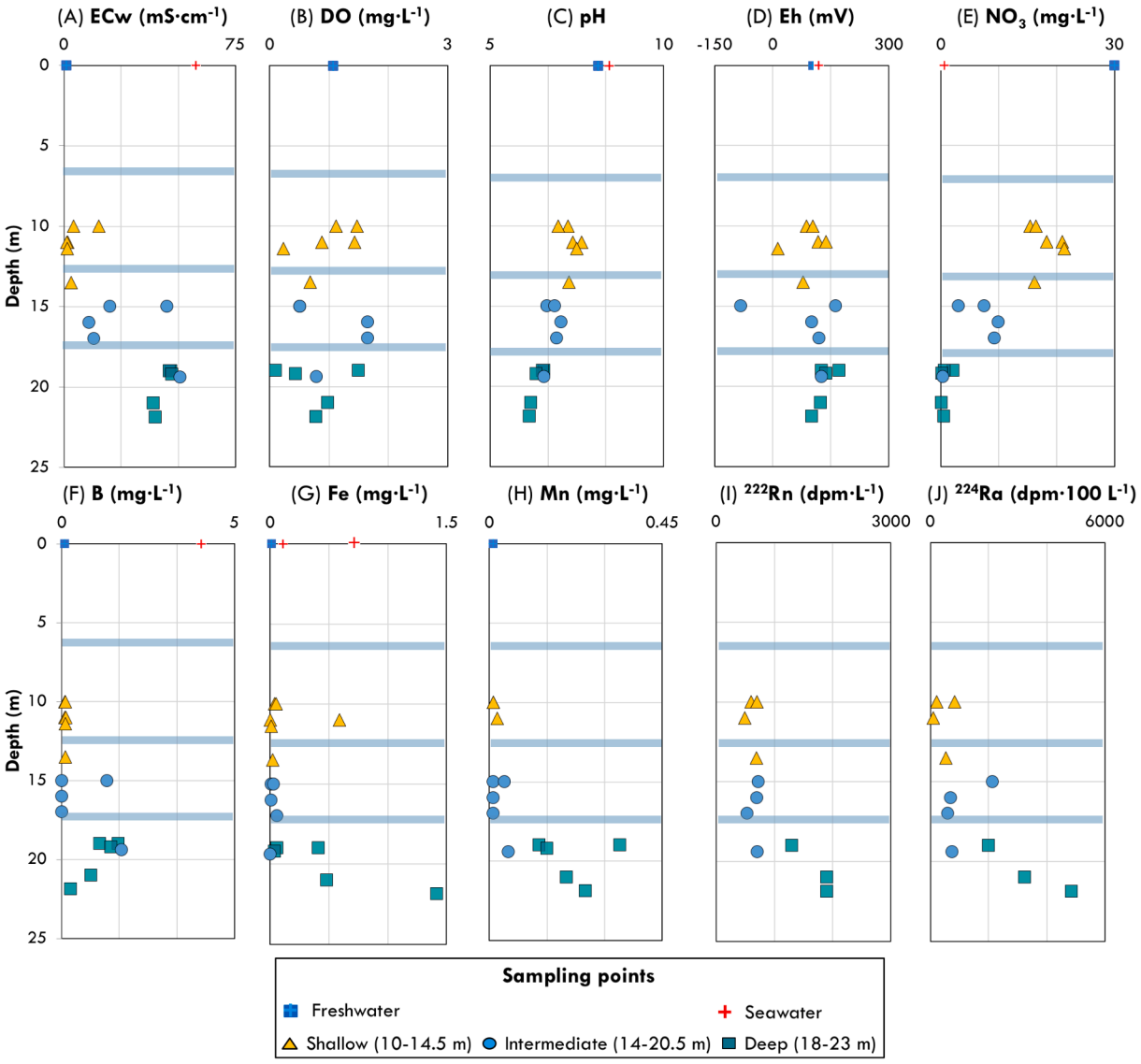

Fig. 7. Evolution of recorded parameters with depth: (A) Electrical conductivity of water, EC_w, (B) Dissolved oxygen, DO, (C) pH, (D) Oxidation-reduction potential, Eh, (E) NO_3, (F) B, (G) Fe, (H) Mn, (I) ^{222}Rn and (J) ^{224}Ra. Sampling points have been grouped depending on the piezometer slotted interval depth in: Shallow, Intermediate and Deep to facilitate the interpretation. The trace of the silty zones is marked in blue. (For interpretation of the references to colour in this figure legend, the reader is referred to the web version of this article.)

(Fig. 8G) are relatively close to the theoretical mixing line which suggests no dissolution or precipitation of calcite or other carbonate minerals. Na and K depletion (Fig. 8B and C respectively) coincides with Ca and Mg enrichment (Fig. 8A and F respectively). In fact, the sum of these four ions lies on the mixing line (Fig. 8E). This indicates that cation exchange is an important reaction. Also, NO_3 (Fig. 7E) and SO_4 are depleted (Fig. 8D), which may be attributed to organic matter oxidation and/or gypsum precipitation. This will be further discussed in Section 4.2.

$\delta^{18}O$ ranges from −5.9‰ (N4-15) to 0.7‰ (seawater sample) and, δD present values from −38.0 (N2-15, inland borehole) to 7.5‰ (seawater sample) (Fig. 8I). Upstream freshwater has a value of −5.2 for $\delta^{18}O$ and −32.6 ‰ for δD. All the values are below the local meteoric water line (LMWL), defined by Neal et al. (1992), and plot along the freshwater – seawater mixing line. This enables calculation of the percentages of mixing between fresh groundwater and seawater (Table S3, SM). Isotopic values obtained from the shallower boreholes (between 10 and 19 m depth) plot along the global meteoric water line (GMWL), whereas samples from 19 to 22 m depth are below (Fig. 8I). Values from the deeper piezometers (from 19 to 22 m depth) and intermediate piezometers near the sea (PP20B and N1-20) are the most affected by seawater intrusion, and therefore tend to be more enriched in $\delta^{18}O$ and δD relative to shallower boreholes (from 10 to 19 m depth).

The concentrations of ^{224}Ra and ^{222}Rn measured at different piezometers spanned a wide range and displayed different behavior (Fig. 7I, J and Fig. 8H). The concentrations of both isotopes in groundwater are significantly higher than those in seawater, as a consequence of the continuous production from their radioactive parents (^{228}Th and ^{226}Ra, respectively) in the aquifer solids. ^{222}Rn concentrations are relatively constant at 500–700 dpm·L^{-1} for the shallower and intermediate piezometers, but the concentrations increase significantly at the deeper part of the aquifer (up to 2000 dpm·L^{-1}). Instead, Ra correlates with Cl^- in low to moderate salinity samples, as expected given the sensitivity of Ra mobility with salinity discussed in the Introduction. However, this dependence is reversed for high salinity samples (Fig. 7J and Fig. 8H). The lowest ^{224}Ra concentrations measured in deep saline samples coincides with the highest Cl concentration. The high Ra samples correspond to zones with lowest pH (6.4). Note also that relatively high Ra

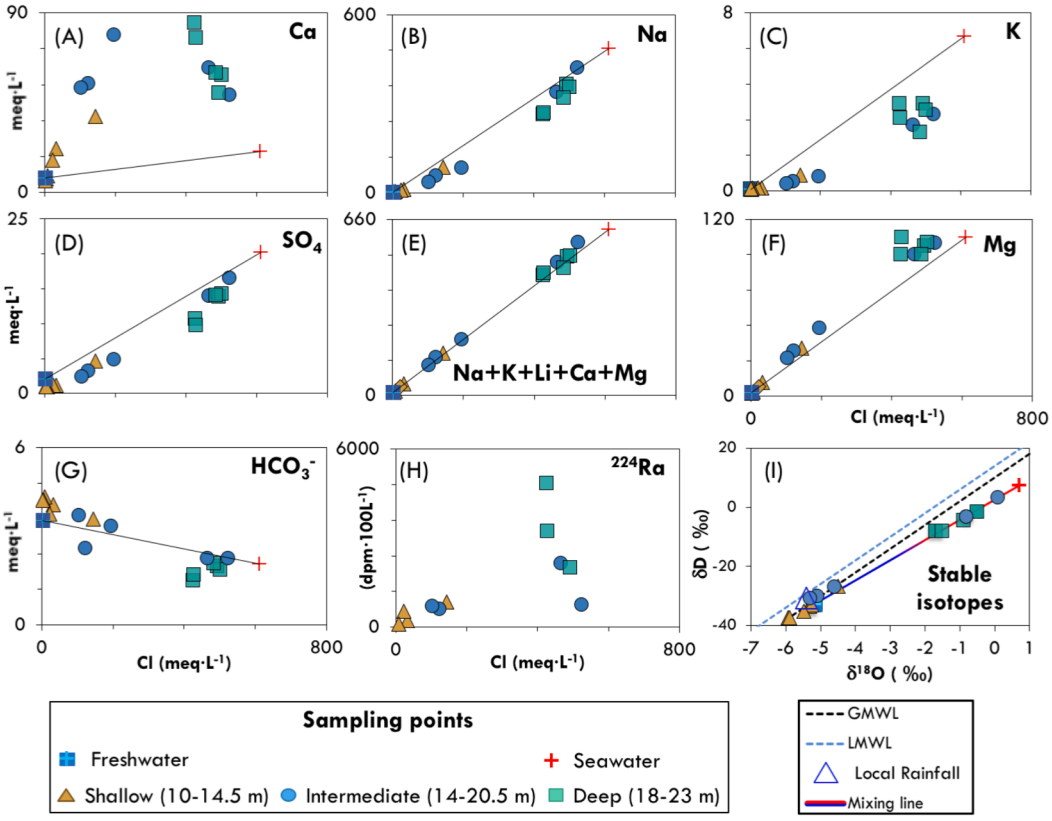

Fig. 8. Hydrochemical characterization: Ionic relationships of the different elements (in meq·L^{-1}) with chloride. (A) Ca, (B) Na, (C) K, (D) SO_4, (E) Na + K + Li + Ca + Mg, (F) Mg, (G) HCO_3^-, (H) ^{224}Ra. (I) $\delta^{18}O$ vs δD values.

concentrations, comparable to those of high salinity samples, are obtained in some of the low salinity samples. It is clear that Ra concentrations are affected by mechanisms other that salinity dependent sorption.

4. Discussion

In this section, we discuss the benefit of combining the different types of techniques that led to the conceptual model of the Argentona experimental site (Fig. 9), which may be extrapolated to other coastal alluvial aquifers.

4.1. Multiscale integration: Role of local heterogeneities in SWI and SGD

The composition and structure of the aquifer resulted from combining lithological and geochemical analyses of the extracted cores, the different geophysical techniques and the hydraulic response. In particular, the correlation between geophysical downhole measurements unveiled the lateral continuity of finning-upwards sequences interspersed by 3 silty layers. Nevertheless, the first and third of these layers had gone unnoticed during the first core descriptions. We discuss here how we came to conclude they are continuous and the implications for SWI and SGD.

Analysis performed at small scale in each of the sequences facilitated the interpretation of the origin of the deposits. The gradation is the result of ephemeral stream dynamics. High energy currents mobilize coarser unconsolidated materials from the headwater and transport them to the depositional zone closer to the sea, developing continuous layers (Bull, 1997). Progressive energy reduction causes the stream to transport finer sediments, which forms the basis of the silty layers that extend respectively between: 7–8 m, 12–13 m and 17–18 m (Fig. 9A). The silt layers are a testament to the low energy of the stream.

All silt layers were marked by higher magnetic susceptibility (MS) and bulk radium concentration in the core samples (Fig. 9A). The anomaly in magnetic susceptibility was also detected in MS downhole measurements (Fig. 9B). Thus, MS logging identified the first and the third silt layers (layer type 1, Fig. 9A), while the second silt layer (layer type 2, Fig. 9A) stands out more in spectral gamma ray (SGR) logs. In fact, both types of measurements provide complementary geochemical information regarding the sediments: MS reveals the presence of magnetic minerals linked to Fe and Mn, whereas SGR spotted K-rich minerals. Acid digestion analyses present peaks of Mn, Fe at these specific fine-grained layers (Fig. 4B and D). Also, bulk radium concentration peaks indicate radionuclides adsorbed to the surface of the silt grains. Particularly at the second silt layer where higher CEC was recorded (Fig. 9A). Furthermore, at depth (21 m) a lithological change is detected by the high BET, CEC, Th/K, and illite percentage (Fig. 9A).

The vertical distribution of layers has an impact on aquifer groundwater flow, SWI and SGD. Both short pumping tests and the tidal method revealed high transmissivity zones located at the intermediate and upper layers of the aquifer and a somewhat less transmissivity zone below 18 m (Fig. 9C). Additionally, within the 7 identified sequences, the vertical variability of hydraulic conductivities (K) calculated from core samples reflects the grain size gradation with depth, showing further lower transmissivities at depth.

Tidal response measured at the site showed very short lags (i.e., very fast response), especially for 20 m deep observation wells (circles in Fig. S2B, Supplementary Material). This suggests, at first sight, a high connectivity with the sea but is inconsistent with a high damping. We can only attribute this short lag to HM response, which is driven by the time derivative of sea level and thus tends to be one quarter of a period shorter than hydraulic response (Guarracino et al., 2012). Lag dampening results, which are aligned when plotted versus distance to the coast (Fig. S2B, Supplementary Material), without passing through the

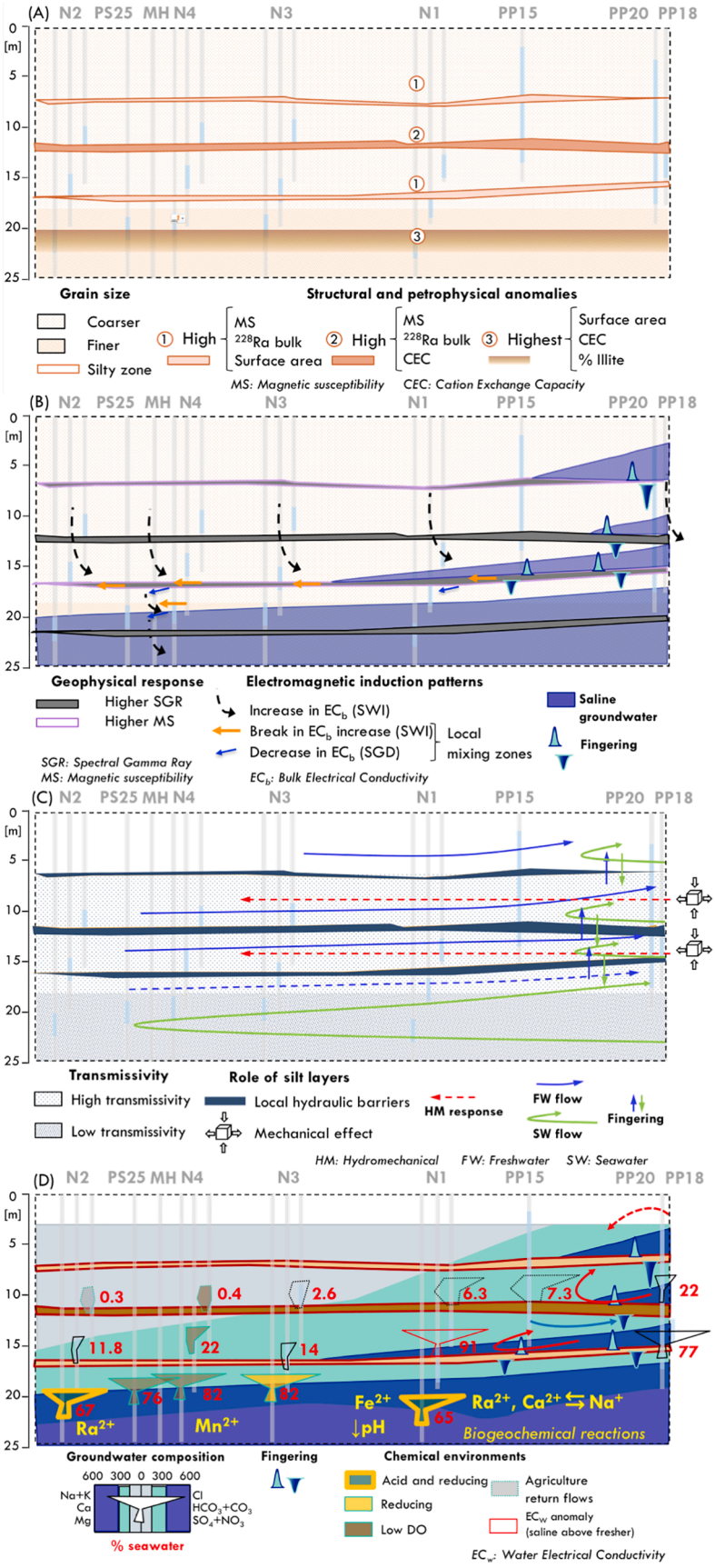

Fig. 9. Contribution to proposed conceptual model from each pillar: (A) Geology (structure and mineral composition), (B) Geophysics (allows extrapolating structure and highly dynamic salinity patterns) , (C) Hydraulics (mechanical response implies offshore continuity of layers) and (D) Hydrochemistry (high reactivity and intense mixing). All of them together lead us to conjecture the proposed double fingering SGD-SWI exchange. EC_b: Bulk electrical conductivity of the formation, MS: magnetic susceptibility, SGR: spectral gamma-ray, HM: hydromechanical, FW: freshwater, SW: seawater, EC_w: Water electrical conductivity.

origin, support the HM response interpretation. Damping results would have passed through the origin if the aquifer had behaved as unconfined, which is the expectation for alluvial aquifers. Therefore, these observations imply that our experimental site behaves like a confined or semi-confined multi-aquifer system for the monitored depths, certainly below the sea for the HM response to be relevant. This result complements geological and geophysical data, as it indicates the continuity of the silt layers beyond the experimental site.

The effect of alternating layers and their different hydraulic conductivities affect the SWI and SGD distribution. This is especially relevant for high transmissivity layers, which are the ones that we are sure are connected offshore. In fact, bulk electrical conductivity (EC_b) tends to increase drastically below 15 m (Fig. 9B), where the high transmissivity intermediate zone is identified. By default, we would have attributed such a high increase in EC_b to a SWI wedge. However, this EC_b increase is not monotonous in depth (Fig. 9B) with lower EC_b below the 17 m silt layer and it is highly variable both in space and time (Palacios et al., 2020). We attributed these EC_b fluctuations to fresher groundwater discharge below the silt layers. The integration of geophysical data with hydrochemical analysis confirmed this hypothesis (see Stiff diagrams in Fig. 9D and EC_b profiles N1 in Fig. 5). That is, fresh water appears to discharge at three depths (below every silt layer) besides the surface discharge. Having such a complex discharge in an aquifer that was initially considered homogeneous is in itself a surprise. It forces us to assume that freshwater SGD does not occur mainly at the shore, but diffused over a long, albeit unknown, offshore length. The alternations of dense saline water above silt layers with less dense brackish water below them lead to Rayleigh–Taylor instability. That is, saltwater tends to sink down, whereas fresher water tends to float upwards, which favors the development of fingers. Density driven fingering is well known for temperature dependent problems (Elder, 1967), and it has been extensively studied for composition dependent density problems during geological storage of CO_2, where fingering enhance CO_2 dissolution rate (Riaz et al., 2006; Hidalgo and Carrera, 2009). We conjecture that the unstable situation we have observed causes discharge to occur through fingers that are intermittent both in space and time (Fig. 9). This explains why we were unable to sample freshwater (or mixed seawater-freshwater) SGD offshore. It also explains the unusually high reactivity of the site.

The finding about the highly dynamic nature of SWI is further supported by two subtle features of the EC_b, logs in the freshwater zone (a zoom of these logs is shown in Fig. 10). First, EC_b displays a weak but yet clear increasing downwards trends. Second, beyond this trend, isolated EC_b maxima are associated to silt layers or (N2 and N3) the aquifer top. The maxima in silt layers might be attributed to surface electrical conduction (Waxman and Smits, 1968), but the magnitudes of the increase (5 to 20 mS/cm) are too high for surface conduction. Instead, we conjecture that both observations reflect trapped by relict salinity from past intrusion or surface seawater flooding events (storm surges) (Illangasekare et al., 2006). Both may occur. On the one hand, we have observed surface flooding by waves during storms and may well explain high EC_b near the surface at some wells. On the other hand, the homogeneity of the maxima at the silt layer suggest that the original salinity may have been caused by past intrusion events (i.e., inland advance of the SWI wedge during long drought periods).

The summary of all observations led us to conjecture the conceptual model of Fig. 9. It could be rightly argued that we have not observed either the diffuse freshwater (actually mixed FW-SW) discharge far offshore, or the fingers. However this model is consistent with sandbox experiments of Castro-Alcalá et al. (2012) who found that relatively minor heterogeneities may cause the saltwater wedge to split. It is also consistent with numerical results from Michael et al. (2016) who simulated deep freshwater discharge under minor silt layers. But, while the model is consistent with sand box experiments and numerical simulations, it has never been documented in the field. We conjecture this model on the basis of the observation of FW (some actually brackish) discharges at several depths near the shore, together the multi-aquifer like tidal response, which ensures the continuity of semi-confined permeable layers. In part, fingering is density fingering is hard to test in the field. The closest field observation is the one by Nield et al. (2008) who attribute to fingering the fluctuations in EC they observed when performing ERT at a sabkha. It could also be argued that that the aquifer is really a multi-aquifer system open to the sea far offshore, which is a frequent paradigm for coastal aquifers. We do not rule out the possibility of some of the highly transmissive layers to be open at some distance offshore, but the fast salinization and freshening of the aquifer requires an equally fast connection to the sea, which would not be possible if the only relevant connection occurred far off-shore.

4.2. *Hydrogeochemical processes in the aquifer*

The complex water circulation pattern discussed above (Fig. 9B) affects hydrochemistry (Fig. 9D). Obviously, the main process is the mixing of FW and SW. We were fortunate at being able to sample the three types of water (FW, nearly 100% SW, and mixed waters, Figs. 5, 7, 8 and 9D). Stable isotopes ($\delta^{18}O$ and δD) revealed that, as expected,

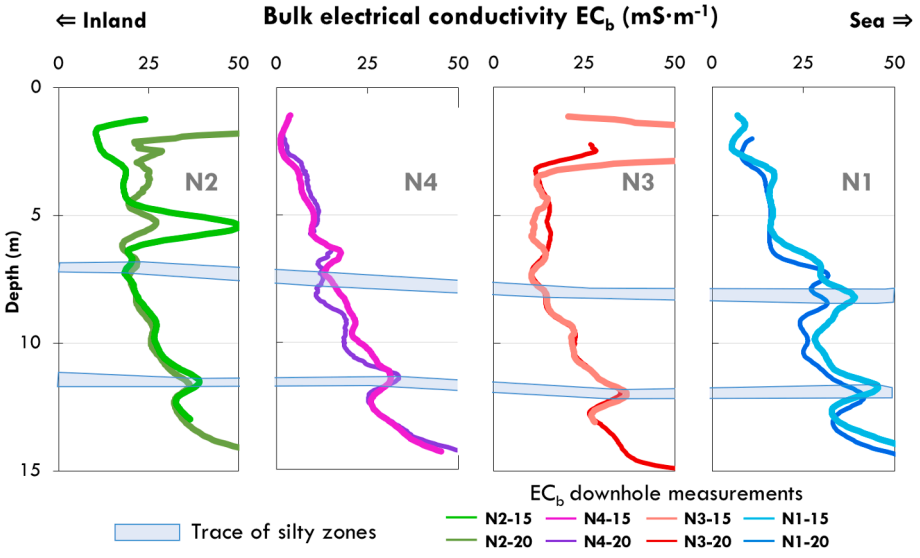

Fig. 10. Zoom of EC_b from electromagnetic induction logs in the freshwater zone (recall that full logs are shown in Fig. 5).

rainfall is the main source of FW. The isotopic signature of shallow samples is similar to that of rainfall, perhaps a bit heavier on the average (Fig. 8I). The remaining samples lie on the mixing line between depleted $\delta^{18}O$ and δD FW and SW.

Several chemical indicators (dissolved oxygen (DO), pH and Eh) indicate redox reactions. DO is low throughout the whole thickness, which indicates organic matter degradation. At the same time, the unusually low pH and Eh reflect anaerobic redox processes such as denitrification and Fe-Mn reduction. Actually, nitrate concentrations tend to decrease with depth (Fig. 9D) and are often accompanied by an increase in boron (Vengosh et al., 2005). In short, denitrification is associated with FW-SW mixing. Moreover, the presence of dissolved Fe and Mn at depth suggests that iron and manganese reduction and mobilization occurs in the SW portion (Fig. 9D). Their absence in mixed samples implies their oxidation and precipitation upon mixing. Both processes contribute to the unusually low pH (Fig. 7C and 9D).

The plots of most solutes versus chloride highlight the occurrence of several chemical reactions other than redox processes (Fig. 8A-H). With the possible exception of alkalinity (Fig. 8G), no compound displays the conservative behavior of $\delta^{18}O$ and δD and/or plot along the conservative mixing line between the two assumed end-members (upstream fresh groundwater and seawater). Several indicators, such as the slightly high nitrate concentrations (see Fig. 7E) and the low Cl/Br ratio of 95 measured in the shallowest boreholes, can be interpreted as characteristic of agriculture-return flows (Bear et al., 1999). Here, they can be linked to the agricultural activities that take place upstream (Rufí-Salís et al., 2019).

The two most significant deviations from the conservative mixing line are Ca and ^{224}Ra (Fig. 8A and H). In fact, Ca concentrations are remarkably high for a non-carbonate coastal aquifer (Table S3, Supplementary Material), only second to those of Santucci et al. (2017), who also dealt with siliciclastic coastal deposits, or the values obtained by Boluda-Botella et al. (2008) during SWI laboratory experiments. Increases of Ca have been traditionally attributed to the dissolution of carbonate and/or gypsum cement contained in the sandy matrix, or to the hydrolysis of plagioclase and hornblende (Santucci et al., 2017). Although carbonate dissolution might be possible, the alkalinity does not deviate much from conservative mixing and pH is rather low. Both observations imply that carbonate dissolution is not an important factor. Also, gypsum dissolution is unlikely because SO_4 data (Fig. 8D) fall below the mixing line, which implies precipitation rather than dissolution. Another possible source of Ca might be the occurrence of granitic saprolites characteristic of this region (Bech, 1977).

We attribute the large deviations of Ca and ^{224}Ra from the mixing line to cation exchange driven by SW inflow (Xue et al., 2000; Liu et al., 2017; Zhang et al., 2017). In this regard, Ca and ^{224}Ra enrichments (Fig. 8A and H and Fig. 9D for Ca) are both linked to Na and K depletion (Fig. 8B and C and Fig. 9D). The near absence of Na in groundwater is also noted by the low Na/Cl ratios (less than 0.86) (Custodio and Bruggeman, 1987). These observations highlight that the main reaction here is cation exchange (Fig. 9D). Cation exchange is also validated by the behavior of the sum of all cations (Fig. 8E), which plots as conservative. Also, the shape of Stiff diagrams show Ca concentrations greater than Na (Fig. 9D), despite Na is the predominant cation in SW, which also confirms cation exchange between Na and Ca on aquifer solids. Therefore, dissolution and/or precipitation reactions are not the main reactions controlling cation concentration variations. Moreover, in the lower part of the aquifer we found that the lowest Na concentration (Fig. 8B) corresponds to the highest Ca (Fig. 8A) and ^{224}Ra concentrations (Fig. 8H and 9D).

Grain scale analyses in borehole N1-25 (Section 2.2) enabled us to relate high ^{224}Ra activities in groundwater with the geochemical properties of the sediment (Fig. 3), and interpret groundwater activities in other zones of the site. Maximum ^{224}Ra activities were related to highest BET surface area and CEC (see Fig. 3B and C), mostly controlled by a high exchangeable Na (Fig. 3D). So, at depth, where salinity is high, high radium can be attributed to desorption from sediment surfaces, due to the known tendency of Ra to be exchanged by Na (Webster et al., 1995). This finding is supported by geochemical data. We have identified a non-negligible CEC increase (Fig. 3C) at one of the continuous silt layers (12 m depth). Since freshwater is dominant at this depth, ^{226}Ra and ^{228}Ra activity remains high in the sediments (Fig. 3F). This higher activity could be linked to the presence of manganese oxides such as in the shallow silt layers (recall that we interpreted that Mn is mobilized at depth but is oxidized and precipitates in the mixing zone), where both MnO (Fig. 4B) and magnetic susceptibility maxima measured in samples (Fig. 3E) correlate with radium content (Fig. 3F). This correlation is not surprising, since MnO enables the capture of Ra by adsorption (Gonneea et al., 2008). Nevertheless, broad application of the magnetic susceptibility (MS) logging tool might allow us to localize radionuclides on a larger scale, which would confirm the potential of this hypothesis to have new application in the field.

We also found some high salinity zones that do not present the highest ^{224}Ra concentration (Fig. 8H). In order to explain this, further integration of the hydrochemical data with the structure and flow within the aquifer provided by the geological and hydraulic assessment was needed. Areas with ^{224}Ra concentrations lower than expected (Fig. 7J and 8H) coincided with the most transmissive areas, which consist of sands and gravels (Figs. 2 and 3A) represented by an increase of the grain size, low Th/K ratio (Fig. S1B), and high hydraulic conductivity and transmissivity. Larger grain size reduces the surface area available for chemical reactions and thus a reduction of ^{224}Ra desorption to the liquid phase (Luo et al., 2019; Li et al., 2021). Alternatively, we attributed Ra enrichment in lower saline areas to less transmissive zones that are rich in parent radionuclides and may provide a suitable environment for ^{224}Ra accumulation in water via parent production and alpha recoil. In summary, Ra desorption is a dominant mechanism but not the only one. Variability in CEC, presence of MnO and pH variability also contribute to explain the variability of Ra in the aquifer. Moreover, in the deeper part of the aquifer, where we identified finer grained sediments linked to the weathered granite, Rn concentrations tended to increase in groundwater (Fig. 7I), which reflects the occurrence of the same type of lithology (see U content in Fig. S1, Supplementary Material).

The identification of the different hydraulic conductivity zones together with the detailed geochemical characterization of the aquifer helped to characterize groundwater hydrochemistry, the most important reactions and the general trend of Ra activities. Still, the intensity of reactions is somewhat surprising. We conjecture that high reactivity reflects the active mixing processes activated by the fingering upwards of discharging freshwater and the fingering downwards of intruding seawater (Fig. 9D). Unfortunately, the complexity of the aquifer makes the geochemical interpretation complicated even when combined with different geological techniques, and requires further geochemical modeling to improve identification and quantification of reactions.

4.3. Advantages of the four-pillar approach

We argue that the four pillars of hydrogeology (geology, hydraulics, hydrogeochemistry and geophysics) should be used whenever a detailed and thorough understanding of processes is sought, but especially if they are complex. Ideally, they should be integrated by modeling. The Argentona case illustrates the advantages of the four pillars approach. Unfortunately, modeling falls beyond the scope of our paper, not to mention that validating the conjecture of double (upwards and downwards, Fig. 9D) fingering process we are proposing requires a singular modeling effort.

The first benefit of the four pillars approach came with the initial conceptual model, largely based on core descriptions. Hydraulic (tidal response, Goyetche et al., in press) and geophysics (CHERT, Palacios et al., 2020) soon pointed that the aquifer was behaving as a multi-aquifer system, which required revising the initial core descriptions. The

revised descriptions indeed identified relatively thin silt layers at 7 and 17 m depths that had been initially discarded as irrelevant. The need to revise the initial geology in response to observations from other kinds of data is not unusual. In fact, it is probably more the rule than the exception (Bredehoeft, 2005). Still, establishing the continuity of these layers and their role required the four types of data, as discussed extensively in the two previous sections.

A second benefit of the four pillars lies on the possibility of integrating processes that occur at a small scale into the site scale picture. This benefit becomes apparent, for instance, on the interpretation of aqueous Ra concentrations, which depend on both large and small-scale processes. Large scale salinity patterns control the overall mobility of Ra. These patterns are generally derived, and they were derived here, from the EC_w water samples, but extending these point measurements to the whole vertical section was facilitated by CHERT and hydraulic understanding. Induction logs also proved extremely useful. Given the difficulty of maintaining CHERT electrodes operational for extended durations (salinity and ERT currents favor their corrosion), induction logs may be more practical than CHERT, albeit less extensive, for long term SWI monitoring. Small scale geochemical data (grain scale mineralogy) together with SGR logs helped in understanding the moderately high Ra concentrations in the FW zone. Note, however that some small-scale features (presence of MnO or somewhat high salinity at the silt layers) may have been caused by large-scale (water circulation) long-term (sporadic aquifer salinization) features.

The type of characterization performed at the Argentona site (notably the density of boreholes with short screened intervals) cannot be achieved at the regional scale, usually required for coastal aquifer management. Still, we would argue that, beyond the specific lessons learned at Argentona, some observations on the four pillars approach can be generalized. We recommend placing emphasis in acknowledging heterogeneity by means of detailed cores geological description, geochemistry and geophysical logs, water sampling and both pumping and tidal tests, which can be performed at a moderate cost. These, together with ERT, should help in understanding and controlling SWI and SGD at large scale coastal aquifers.

5. Synthesis and conclusions

Traditional techniques (core descriptions, hydraulic tests, head monitoring, and hydrochemical sampling) forged the way for aquifer characterization, significantly improved the understanding of the Argentona site. The integration of disparate techniques enabled the identification of sedimentary origin and mineralogy, as well as the localization of continuous silt layers (also using SGR logs) between sandy materials affecting seawater intrusion, as shown by geophysical data and groundwater hydrochemistry. The hydraulic discontinuities were identified by combining laboratory and field scale traditional measurements. Hydraulic conductivities obtained from both grain size distribution and pumping test, highlighted the changes in hydraulic conductivity as well as its tendency to decrease with depth. Analysis of tidal response in the Argentona experimental site revealed that the aquifer behaves as a multi-aquifer system. The silt layers explain why the conventional unconfined character attributed to alluvial aquifers is not verified here. The presence of hydraulic barriers governs the SWI-SGD dynamics and interface localization of the aquifer.

All this work leads to three types of conclusions: conceptual, methodological and operational. From the conceptual point of view, it is clear that the main conclusion is related to the SWI-SGD exchange mechanisms.

SWI and SGD, separated by thin silt layers, take place at several depths despite the fact that we are studying a relatively homogeneous 22 m thick "unconfined" aquifer. We also propose a double fingering mechanism which could explain the observed patterns: fresh-brackish water fingering its way upwards towards the sea because it is lighter than saline water, and seawater fingering down because it is denser than fresh-brackish water. These two types of fingers do not need to occur simultaneously. Seawater may enter preferentially during dry periods, when aquifer heads drop. And, reversely, fresh water outflow may dominate during wet periods, when aquifer heads build up. Two implications of this model are that (1) the outflow resistance is much larger than in the traditional SWI paradigm, and (2) SGD tends to occur offshore even in this apparently unconfined aquifer.

A conceptual consequence of this mechanism is that the mixing zone at Argentona (and, we suspect, other alluvial coastal aquifers) is extremely active from the chemical point of view. Beyond the expected cation exchange mechanisms, we have found Fe and Mn reduction in the SW portion of the aquifer. We have found that the mobilized Fe and Mn tend to oxidize and precipitate when mixed with FW, so that they can only reach the sea as recirculated SW discharge. We have observed significant denitrification. And, finally, we conclude that Ra concentrations are controlled by many other factors other than salinity (pH, geological variability, presence of MnO), which make it difficult to define a Ra concentration representative of the discharging groundwater.

We have reached a number of methodological findings. The main one is that the multi-scalar and multidisciplinary approach used to characterize the Argentona research site allowed us to integrate geological, geophysical, hydraulic and hydrochemical data. This combined effort enabled the interpretation of the measured datasets that led to the above conceptual model of the experimental site. Grain-scale analyses on discrete samples enabled localization of geochemical hotspots. We found correlations between geochemical parameters (BET, CEC), mineral composition, and grain size, such as the high activity of ^{226}Ra coupled with MnO and magnetic susceptibility maxima. These correlations deserve further exploration. It is clear that the level of detail achievable at a research site cannot be realized at regional aquifers. Still, our methodological findings may facilitate characterizing SWI and SGD at greater scales with more realistic densities of boreholes.

Finally, from an operational point of view, some of our findings may be relevant both for controlling SWI by water managers and understanding SGD by water scientists. Specifically, the fact that an apparently homogeneous unconfined aquifer behaves like a multiaquifer system suggests that freshwater can be extracted during short periods of time. This observation is key to investigating the heterogeneity of shallow alluvial aquifers, since resistance to SWI and flow disturbance may be greater than expected in this kind of aquifers. By the same token, we conjecture that FW discharge will often be diffuse and will also occur further offshore than explained by the conventional SWI paradigm. Finally, the contribution of the Argentona conceptual model together with the ensemble of techniques may serve as a basis for further investigations on the coupling of SWI and SGD in alluvial coastal aquifers.

CRediT authorship contribution statement

Laura Martínez-Pérez: Conceptualization, Methodology, Writing – original draft, Investigation, Resources, Visualization. **Linda Luquot:** Data curation, Conceptualization, Methodology, Writing – original draft, Project administration, Funding acquisition. **Jesús Carrera:** Supervision, Conceptualization, Methodology, Writing – original draft. **Miguel Angel Marazuela:** Data curation, Conceptualization, Writing – original draft. **Tybaud Goyetche:** Data curation, Conceptualization, Methodology, Writing – original draft. **María Pool:** Conceptualization, Methodology, Supervision. **Andrea Palacios:** Conceptualization, Methodology, Writing – review & editing. **Fabian Bellmunt:** Conceptualization, Methodology, Investigation. **Juanjo Ledo:** Conceptualization, Methodology, Investigation, Writing – review & editing. **Nuria Ferrer:** Resources. **Laura del Val:** Resources, Investigation, Writing – review & editing. **Philippe A. Pezard:** Investigation, Methodology, Conceptualization, Writing – review & editing. **Jordi García-Orellana:** Resources, Investigation, Writing – review & editing, Conceptualization. **Marc Diego-Feliu:** Resources, Investigation, Writing – review & editing,

Conceptualization. **Valentí Rodellas:** Resources, Investigation, Writing – review & editing. **Maarten W. Saaltink:** Writing – review & editing. **Enric Vázquez-Suñé:** Supervision, Writing – review & editing, Conceptualization. **Albert Folch:** Methodology, Supervision, Project administration, Funding acquisition, Supervision, Writing – review & editing.

Declaration of Competing Interest

The authors declare that they have no known competing financial interests or personal relationships that could have appeared to influence the work reported in this paper.

Acknowledgements

We acknowledge the contribution of all the members of the MEDISTRAES I, II and III project, from the Groundwater Hydrology Group of the Technical University of Catalonia (UPC) and the Spanish National Research Council (CSIC), the Autonomous University of Barcelona (UAB), the University of Barcelona (UB), the Geosciences Montpellier Laboratory, CNRS and the University of Rennes, for their support during experimental laboratory tests, the Argentona site creation, the setup of the electrodes during boreholes installation and for ensuring site maintenance. The final manuscript was significantly improved by critical, but constructive comments by two anonymous reviewers.

This work was funded by the project PID2019-110212RB-C21, CGL2016-77122-C2-1-R/2-R and PID2019-110311RB-C22 of the Spanish Government and the project TerraMar (grant no. ACA210/18/00007) of the Catalan Water Agency. We would like to thank SIMMAR (Serveis Integrals de Manteniment del Maresme) and the Consell Comarcal del Maresme in the construction of the research site. This study contributes to the work carried out by the GHS (2017 SGR 1485) and MERS research group (2017 SGR 1588) for additional funding. M. Diego-Feliu acknowledges the economic support from the FI-2017 fellowships of the Generalitat de Catalunya autonomous government (2017FI_B_00365). V. Rodellas acknowledges financial support from the Beatriu de Pinós postdoctoral program of the Generalitat de Catalunya autonomous government (2019-BP-00241) The co-author Albert Folch is a Serra Húnter Fellow.

Appendix A. Supplementary material

Supplementary data to this article can be found online at https://doi.org/10.1016/j.jhydrol.2022.127510.

References

Abarca, E., 2006. Seawater Intrusion in Complex Geological Environments. PhD Thesis. Universitat Politècnica de Catalunya.
Andersen, M.S., 2005. Geochemical processes and solute transport at the seawater/freshwater interface of a sandy aquifer. Geochim. Cosmochim. Acta 69 (16), 3979–3994.
Arabelos, D., Papazachariou, D., Contadakis, M., Spatalas, S., 2011. A new tide model for the Mediterranean Sea based on altimetry and tide gauge assimilation. Ocean Sci. 7 (3), 429.
Archie, G.E., 1942. The electrical resistivity log as an aid in determining some reservoir characteristics. Trans. AIME 146 (01), 54–62.
Bakker, M., Miller, A.D., Morgan, L.K., Werner, A.D., 2017. Evaluation of analytic solutions for steady interface flow where the aquifer extends below the sea. J. Hydrol. 551, 660–664.
Bear, J., Cheng, A.H.-D., Sorek, S., Ouazar, D., Herrera, I., 1999. Seawater intrusion in coastal aquifers: concepts, methods and practices, 14. Springer Science & Business Media.
Bech, J., 1977. El factor climático en la edafogénesis del Maresme (Barcelona). Revista de geografia 11 (1), 37–61.
Bech, J., Cardus, J., Lasala, M., Bouleau, A., Lamouroux, M., Quantin, P., Ségalen, P., 1983. Etude des sols formés sur les granites du Maresme (Catalogne, Espagne). Cahiers de l'ORSTOM, sér. Pédologie 209–221.
Beck, A.J., Cochran, M.A., 2013. Controls on solid-solution partitioning of radium in saturated marine sands. Mar. Chem. 156, 38–48.
Beusen, A., Slomp, C., Bouwman, A., 2013. Global land–ocean linkage: direct inputs of nitrogen to coastal waters via submarine groundwater discharge. Environ. Res. Lett. 8 (3), 034035.
Boluda-Botella, N., Gomis-Yagües, V., Ruiz-Beviá, F., 2008. Influence of transport parameters and chemical properties of the sediment in experiments to measure reactive transport in seawater intrusion. J. Hydrol. 357 (1–2), 29–41.
Bredehoeft, J., 2005. Modeling: the conceptualization problem-surprise. Hydrogeol. J. 13 (1), 37–46.
Brunauer, S., Emmett, P.H., Teller, E., 1938. Adsorption of gases in multimolecular layers. J. Am. Chem. Soc. 60 (2), 309–319.
Bull, W.B., 1997. Discontinuous ephemeral streams. Geomorphology 19 (3–4), 227–276.
Burnett, W.C., Aggarwal, P.K., Aureli, A., Bokuniewicz, H., Cable, J.E., Charette, M.A., Kontar, E., Krupa, S., Kulkarni, K.M., Loveless, A., et al., 2006. Quantifying submarine groundwater discharge in the coastal zone via multiple methods. Sci. Total Environ. 367 (2), 498–543.
Burnett, W.C., Taniguchi, M., Oberdorfer, J., 2001. Measurement and significance of the direct discharge of groundwater into the coastal zone. J. Sea Res. 46 (2), 109–116.
Carr, P., Van Der Kamp, G., 1969. Determining aquifer characteristics by the tidal method. Water Resour. Res. 5 (5), 1023–1031.
Carrera, J., Hidalgo, J.J., Slooten, L.J., Vázquez-Suñé, E., 2009. Computational and conceptual issues in the calibration of seawater intrusion models. Hydrogeol. J. 18 (1), 131–145.
Castro-Alcalá, E., Fernàndez-Garcia, D., Carrera, J., Bolster, D., 2012. Visualization of mixing processes in a heterogeneous sand box aquifer. Environ. Sci. Technol. 46 (6), 3228–3235.
Cerdà-Domènech, M., Rodellas, V., Folch, A., Garcia-Orellana, J., 2017. Constraining the temporal variations of Ra isotopes and Rn in the groundwater end-member: Implications for derived SGD estimates. Sci. Total Environ. 595, 849–857.
Chidichimo, F., De Biase, M., Rizzo, E., Masi, S., Straface, S., 2015. Hydrodynamic parameters estimation from self-potential data in a controlled full scale site. J. Hydrol. 522, 572–581.
Cho, H.-M., Kim, G., Kwon, E.Y., Moosdorf, N., Garcia-Orellana, J., Santos, I.R., 2018. Radium tracing nutrient inputs through submarine groundwater discharge in the global ocean. Sci. Rep. 8 (1), 2439.
Church, T.M., 1996. An underground route for the water cycle. Nature 380 (6575), 579–580.
Cisteró, X.F., Camarós, J.G., 2014. Les rierades al Maresme. Atzavara, L' 23, 61–79.
Clark, I.D., Fritz, P., 2013. Environmental Isotopes in Hydrogeology. CRC Press.
Cook, P.G., Rodellas, V., Stieglitz, T.C., 2018. Quantifying surface water, porewater, and groundwater interactions using tracers: Tracer fluxes, water fluxes, and end-member concentrations. Water Resour. Res. 54 (3), 2452–2465.
Corominas, J., Custodio, E., 1981. Contaminación por nitratos e intrusión marina en el acuífero costero del Maresme (Barcelona). Jorn. Anal, y Evol. Contaminae. de aguas subt. Espana 537–552.
Cripps, A., McCann, D., 2000. The use of the natural gamma log in engineering geological investigations. Eng. Geol. 55 (4), 313–324.
Crossland, C.J., Kremer, H.H., Lindeboom, H., Crossland, J.I.M., Le Tissier, M.D., 2005. Coastal Fluxes in the Anthropocene: The Land-ocean Interactions in the Coastal Zone Project of the International Geosphere-Biosphere Programme. Springer Science & Business Media.
Custodio, E., Bruggeman, G.A., 1987. Groundwater problems in coastal areas. Publication of the IHP Working Group on Changes in the Salt-fresh Water Balance in Deltas. Estuaries and Coastal Zones due to Structural Works and Groundwater Exploitation.
Dearing, J., 1994. Environmental magnetic susceptibility. Using the Bartington MS2 system. Kenilworth, Chi Publ.
Debnath, P., Das, K., Mukherjee, A., Ghosh, N.C., Rao, S., Kumar, S., Krishan, G., Joshi, G., 2019. Seasonal-to-diurnal scale isotopic signatures of tidally-influenced submarine groundwater discharge to the Bay of Bengal: Control of hydrological cycle on tropical oceans. J. Hydrol. 571, 697–710.
Diego-Feliu, M., Rodellas, V., Alorda-Kleinglass, A., Tamborski, J., van Beek, P., Heins, L., Bruach, J., Arnold, R., Garcia-Orellana, J., 2020. Guidelines and Limits for the Quantification of Ra Isotopes and Related Radionuclides With the Radium Delayed Coincidence Counter (RaDeCC). J. Geophys. Res. Oceans 125 (4).
Diego-Feliu, M., Rodellas, V., Saaltink, M.W., Diego-Feliu, M., Rodellas, V., Saaltink, M. W., Alorda-Kleinglass, A., Goyetche, T., Martínez-Pérez, L., Folch, A., Garcia-Orellana, J., 2021. New perspectives on the use of 224Ra/228Ra and 222Rn/226Ra activity ratios in groundwater studies. J. Hydrol. 596, 126043.
Dulaiova, H., Gonneea, M.E., Henderson, P.B., Charette, M.A., 2008. Geochemical and physical sources of radon variation in a subterranean estuary—Implications for groundwater radon activities in submarine groundwater discharge studies. Mar. Chem. 110 (1–2), 120–127.
Duque, C., Calvache, M.i.L., Pedrera, A., Martin-Rosales, W., López-Chicano, M., 2008. Combined time domain electromagnetic soundings and gravimetry to determine marine intrusion in a detrital coastal aquifer (Southern Spain). J. Hydrol. 349 (3), 536–547.
Duque, C., Knee, K.L., Russoniello, C.J., Sherif, M., Risha, U.A.A., Sturchio, N.C., Michael, H.A., 2019. Hydrogeological processes and near shore spatial variability of radium and radon isotopes for the characterization of submarine groundwater discharge. J. Hydrol. 579, 124192.
Elder, J., 1967. Transient convection in a porous medium. J. Fluid Mech. 27 (3), 609–623.
Elsinger, R.J., Moore, W.S., 1980. 226Ra behavior in the pee Dee River-Winyah Bay estuary. Earth Planet. Sci. Lett. 48 (2), 239–249.

Falgàs, E., 2007. Hydrogeophysics as a multidisciplinary tool on aquifer appraisal: focus on AMT capabilities: Spain, Universidad de Barcelona, Ph. D. Thesis. http://hdl.handle.net/2445/34912.
Falgàs, E., Ledo, J., Benjumea, B., Queralt, P., Marcuello, A., Teixidó, T., Martí, A., 2011. Integrating Hydrogeological and Geophysical Methods for the Characterization of a Deltaic Aquifer System. Surv. Geophys. 32 (6), 857–873.
Ferris, J.G., 1952. Cyclic fluctuations of water level as a basis for determining aquifer transmissibility, US Geological Survey. https://doi.org/10.3133/70133368.
Fetter, C.W., 2018. Applied Hydrogeology. Waveland Press.
Folch, A., del Val, L., Luquot, L., Martinez-Perez, L., Bellmunt, F., Le Lay, H., Rodellas, V., Ferrer, N., Palacios, A., Fernández, S., Marazuela, M.A., Diego-Feliu, M., Pool, M., Goyetche, T., Ledo, J., Pezard, P., Bour, O., Queralt, P., Marcuello, A., Garcia-Orellana, J., Saaltink, M., Vazquez-Suñe, E. and Carrera, J., 2020. Combining Fiber Optic (FO-DTS), CHERT and time-lapse formation electrical conductivity to characterize and monitor a coastal aquifer, https://doi.org/10.1016/j.jhydrol.2020.125050.
Folk, R.L., Ward, W.C., 1957. Brazos River bar [Texas]; a study in the significance of grain size parameters. J. Sediment. Res. 27 (1), 3–26.
Hidalgo, J.J., Carrera, J., 2009. Effect of dispersion on the onset of convection during CO2 sequestration. J. Fluid Mech. 640, 441–452.
Galofre, A., 1969. Estudio hidrogeológico de la cuenca de la Riera dÁrgentona. Tesi de llicenciatura, Universitat de Barcelona. Laboratori de Geomorfologia i Geotectònica.
Gámez, D., Simó, J.A., Lobo, F.J., Barnolas, A., Carrera, J., Vázquez-Suñé, E., 2009. Onshore–offshore correlation of the Llobregat deltaic system, Spain: Development of deltaic geometries under different relative sea-level and growth fault influences. Sed. Geol. 217 (1–4), 65–84.
Garcia-Orellana, J., Rodellas, V., Tamborski, J., et al., 2021. Radium isotopes as submarine groundwater discharge (SGD) tracers. Review and recommendations. Earth-Sci. Rev. 103681.
Gat, J.R. and Gonfiantini, R., 1981. Stable isotope hydrology. Deuterium and oxygen-18 in the water cycle. https://inis.iaea.org/search/search.aspx?orig_q=RN:13677657.
Goldman, M., Kafri, U., 2006. Hydrogeophysical applications in coastal aquifers. Appl. Hydrogeophys. Springer 233–254.
Gonneea, M.E., Morris, P.J., Dulaiova, H., Charette, M.A., 2008. New perspectives on radium behavior within a subterranean estuary. Mar. Chem. 109 (3–4), 250–267.
Goyetche, T., Pool, M., Carrera, J., Diego-Feliu, M., Martínez-Pérez, L., Folch, A., Luquot, L. (in press). Using the tidal method for conceptual model identification and hydraulic characterization at the Argentona site.
Guarracino, L., Carrera, J., Vázquez-Suñé, E., 2012. Analytical study of hydraulic and mechanical effects on tide-induced head fluctuation in a coastal aquifer system that extends under the sea. J. Hydrol. 450–451, 150–158.
Guo, Q., Li, H., Boufadel, M.C., Sharifi, Y., 2010. Hydrodynamics in a gravel beach and its impact on theExxon Valdezoil. J. Geophys. Res. 115 (C12).
Guomin, L., Chongxi, C., 1991. Determining the length of confined aquifer roof extending under the sea by the tidal method. J. Hydrol. 123 (1–2), 97–104.
Hazen, A., 1911. Discussion of "Dams on soil foundations". Trans. Am. Soc. Civ. Eng. 73.
Hesselbo, S.P., 1996. Spectral gamma-ray logs in relation to clay mineralogy and sequence stratigraphy, Cenozoic of the Atlantic margin, offshore New Jersey. In Proceedings of the Ocean Drilling Program: Scientific Results (Vol. 150, p. 411). The Program. http://www-odp.tamu.edu/publications/150_SR/VOLUME/CHAPTERS/sr150_23.pdf.
IGME, 1976. I.G.M.E. (1976). Mapa Geológico de España 1:50.000. Hoja n° 393. Mataró, Segunda Serie, Primera Edición. Instituto geológico y minero de España.
Illangasekare, T., Tyler, S.W., Clement, T.P., Villholth, K.G., Perera, A., Obeysekera, J., Gunatilaka, A., Panabokke, C., Hyndman, D.W., Cunningham, K.J., 2006. Impacts of the 2004 tsunami on groundwater resources in Sri Lanka. Water Resour. Res. 42 (5).
Kim, G., Swarzenski, P., 2010. Submarine Groundwater Discharge (SGD) and Associated Nutrient Fluxes to the Coastal Ocean, pp. 529-538. https://doi.org/10.1007/978-3-540-92735-8_11.
Kiro, Y., Weinstein, Y., Starinsky, A., Yechieli, Y., 2013. Groundwater ages and reaction rates during seawater circulation in the Dead Sea aquifer. Geochim. Cosmochim. Acta 122, 17–35.
Koussis, A.D., Mazi, K., Riou, F., Destouni, G., 2015. A correction for Dupuit-Forchheimer interface flow models of seawater intrusion in unconfined coastal aquifers. J. Hydrol. 525, 277–285.
Li, H., Jiao, J.J., 2001. Tide-induced groundwater fluctuation in a coastal leaky confined aquifer system extending under the sea. Water Resour. Res. 37 (5), 1165–1171.
Li, X., Hu, B.X., Burnett, W.C., Santos, I.R., Chanton, J.P., 2009. Submarine ground water discharge driven by tidal pumping in a heterogeneous aquifer. Ground Water 47 (4), 558–568.
Li, L., Zhong, Q., Du, J., 2021. Radium desorption behavior of riverine suspended sediment: Theoretical and experimental. J. Environ. Radioact. 234, 106644.
Liu, Y., Jiao, J.J., Liang, W., Kuang, X., 2017. Hydrogeochemical characteristics in coastal groundwater mixing zone. Appl. Geochem. 85, 49–60.
Luo, H., Li, L., Wang, J., Zhong, Q., Du, J., 2019. The desorption of radium isotopes in river sediments in Qinzhou Bay. Acta Oceanolog. Sin. 41 (4), 27–41.
Llopis-Albert, C., Pulido-Velazquez, D., 2014. Discussion about the validity of sharp-interface models to deal with seawater intrusion in coastal aquifers. Hydrol. Process. 28 (10), 3642–3654.
Mace, R.E., 2001. Estimating transmissivity using specific-capacity data. Bureau of Economic Geology Vol. 1.
Michael, Post, V.E.A., Wilson, A.M. and Werner, A.D., 2017. Science, society, and the coastal groundwater squeeze. Wiley Online Library, pp. 2610-2617. https://doi.org/10.1002/2017WR020851.
Michael, H.A., Charette, M.A., Harvey, C.F., 2011. Patterns and variability of groundwater flow and radium activity at the coast: a case study from Waquoit Bay, Massachusetts. Marine Chem. 127 (1), 100–114.
Michael, H.A., et al., 2016. Geologic influence on groundwater salinity drives large seawater circulation through the continental shelf. Geophy. Res. Lett. 43 (20), 10,782–710,791.
Mielke, J. E., 1979. Composition of the Earth's crust and distribution of the elements. In: F. R. Siegel (ed.): Review of Research on Modern Problems in Geochemistry. UNESCO Report, Paris, pp. 13-37.
Moore, W.S., 1976. Sampling ^{228}Ra in the deep ocean, Deep Sea Research and Oceanographic Abstracts. Elsevier, pp. 647–651.
Moore, W.S., 2010. The effect of submarine groundwater discharge on the ocean. Annu. Rev. Marine Sci. 2, 59–88.
Moore, W.S., Arnold, R., 1996. Measurement of ^{223}Ra and ^{224}Ra in coastal waters using a delayed coincidence counter. J. Geophys. Res. Oceans 101 (C1), 1321–1329.
Moore, W.S., et al., 1996. Using the radium quartet for evaluating groundwater input and water exchange in salt marshes. Geochim. Cosmochim. Acta 60 (23), 4645–4652.
Moore, W.S., Joye, S.B., 2021. Saltwater intrusion and submarine groundwater discharge: Acceleration of biogeochemical reactions in changing coastal aquifers. Front. Earth Sci. 9, 231.
Neal, C., Neal, M., Warrington, A., Ávila, A., Piñol, J., Rodà, F., 1992. Stable hydrogen and oxygen isotope studies of rainfall and streamwaters for two contrasting holm oak areas of Catalonia, northeastern Spain. J. Hydrol. 140 (1), 163–178.
Nguyen, F., Kemna, A., Antonsson, A., Engesgaard, P., Kuras, O., Ogilvy, R., Gisbert, J., Jorreto, S., Pulido-Bosch, A., 2009. Characterization of seawater intrusion using 2D electrical imaging. Near Surf. Geophys. 7 (5–6), 377–390.
Nield, D.A., Simmons, C.T., Kuznetsov, A.V., Ward, J.D., 2008. On the evolution of salt lakes: episodic convection beneath an evaporating salt lake. Water Resour. Res. 44 (2).
Ozler, M.H., 2003. Hydrochemistry and salt-water intrusion in the Van aquifer, east Turkey. Environ. Geol. 43 (7), 759–775.
Palacios, A., Ledo, J., Linde, N., Luquot, Linda, Bellmunt, Fabian, Folch, Albert, Marcuello, Alex, Queralt, Pilar, Pezard, Philippe A., Martínez, Laura, Bosch, D., Carrera, J., 2020. Time-lapse cross-hole electrical resistivity tomography (CHERT) for monitoring seawater intrusion dynamics in a Mediterranean aquifer. Hydrogl. Earth Syst. Sci. 24 (4), 2121–2139.
Parra, M.M. and Díaz, J.M.M., 2003. Evolución de la contaminacion marina en los acuiferos costeros del Baix Tordera (Barcelona). IGME. https://aguas.igme.es/igme/publica/tiac-01/Area%20V-10.pdf.
Plummer, L., 1975. Mixing of sea water with calcium carbonate ground water. Geol. Soc. Am. Mem. 142, 219–236.
Pool, M., Carrera, J., 2011. A correction factor to account for mixing in Ghyben-Herzberg and critical pumping rate approximations of seawater intrusion in coastal aquifers. Water Resour. Res. 47 (5).
Porcelli, D., Swarzenski, P.W., 2003. The behavior of U-and Th-series nuclides in groundwater. Rev. Mineral. Geochem. 52 (1), 317–361.
Riaz, A., Hesse, M., Tchelepi, H., Orr, F., 2006. Onset of convection in a gravitationally unstable diffusive boundary layer in porous media. J. Fluid Mech. 548, 87–111.
Riba, O., 1997. Les rieres del Maresme. Consideracions sobre aspectes geomorfològics, hidrològics i sedimentològics. Quaderns d'Ecologia Aplicada 14, 123–151.
Rodellas, V., Garcia-Orellana, J., Masqué, P., Feldman, M., Weinstein, Y., 2015. Submarine groundwater discharge as a major source of nutrients to the Mediterranean Sea. Proc. Natl. Acad. Sci. 112 (13), 3926–3930.
Rodellas, V., Garcia-Orellana, J., Trezzi, G., Masqué, P., Stieglitz, T.C., Bokuniewicz, H., Cochran, J.K., Berdalet, E., 2017. Using the radium quartet to quantify submarine groundwater discharge and porewater exchange. Geochim. Cosmochim. Acta 196, 58–73.
Rovere, A., Stocchi, P., Vacchi, M., 2016. Eustatic and Relative Sea Level Changes. Current Climate Change Reports 2 (4), 221–231.
Sanford, W.E., Konikow, L.F., 1989. Simulation of calcite dissolution and porosity changes in saltwater mixing zones in coastal aquifers. Water Resour. Res. 25 (4), 655–667.
Santucci, L., Carol, E., Kruse, E., 2017. Quaternary marine ingressions as indicated by hydrogeochemical evidence in the semi-confined aquifer of the littoral of the Río de la Plata, Argentina. Quaternary Re. 88 (01), 160–167.
Schlumberger, 2009. Log Interpretation Charts—2009 Edition. Schlumberger, Sugar Land.
Serra, O., 2008. Well Logging Handbook. Editions Technip.
Shepherd, R.G., 1989. Correlations of permeability and grain size. Groundwater 27 (5), 633–638.
Slooten, L.J., Carrera, J., Castro, E., Fernandez-Garcia, D., 2010. A sensitivity analysis of tide-induced head fluctuations in coastal aquifers. J. Hydrol. 393 (3–4), 370–380.
Stanjek, H., Künkel, D., 2018. CEC determination with Cu-triethylenetetramine: recommendations for improving reproducibility and accuracy. Clay Miner. 51 (01), 1–17.
Szabo, Z., Zapecza, O.S., 1991. Geologic and geochemical factors controlling uranium, radium-226, and radon-222 in ground water, Newark Basin, New Jersey. Field Studies of Radon in Rocks, Soils, and Water 243–266.
Tamborski, J.J., Cochran, J.K., Bokuniewicz, H.J., 2017. Application of 224Ra and 222Rn for evaluating seawater residence times in a tidal subterranean estuary. Mar. Chem. 189, 32–45.
Tamez-Meléndez, C., Hernández-Antonio, A., Gaona-Zanella, P.C., Ornelas-Soto, N., Mahlknecht, J., 2016. Isotope signatures and hydrochemistry as tools in assessing groundwater occurrence and dynamics in a coastal arid aquifer. Environmental Earth Sciences 75 (9).

Taniguchi, M., Dulai, H., Burnett, K.M., Santos, I.R., Sugimoto, R., Stieglitz, T., Kim, G., Moosdorf, N., Burnett, W.C., 2019. Submarine Groundwater Discharge: Updates on Its Measurement Techniques, Geophysical Drivers, Magnitudes, and Effects. Front. Environ. Sci. 7 (141).

Toro y Llaca, C.d., Vieira, R. and Sevilla, M.J., 1994. Tidal models of the Mediterranean Sea. http://hdl.handle.net/10261/27503.

Vallejos, A., Sola, F., Pulido-Bosch, A., 2015. Processes influencing groundwater level and the freshwater-saltwater interface in a Coastal Aquifer. Water Resour. Manage. 29 (3), 679–697.

Vengosh, A., Kloppmann, W., Marei, A., Livshitz, Y., Gutierrez, A., Banna, M., Guerrot, C., Pankratov, I., Raanan, H., 2005. Sources of salinity and boron in the Gaza strip: Natural contaminant flow in the southern Mediterranean coastal aquifer. Water Resour. Res. 41 (1).

Waxman, M.H., Smits, L., 1968. Electrical conductivities in oil-bearing shaly sands. Soc. Petrol. Eng. J. 8 (02), 107–122.

Webster, I.T., Hancock, G.J., Murray, A.S., 1995. Modelling the effect of salinity on radium desorption from sediments. Geochim. Cosmochim. Acta 59 (12), 2469–2476.

Werner, A.D., Bakker, M., Post, V.E.A., Vandenbohede, A., Lu, C., Ataie-Ashtiani, B., Simmons, C.T., Barry, D.A., 2013. Seawater intrusion processes, investigation and management: Recent advances and future challenges. Adv. Water Resour. 51, 3–26.

Xue, Y., Wu, J., Ye, S., Zhang, Y., 2000. Hydrogeological and hydrogeochemical studies for salt water intrusion on the south coast of Laizhou Bay, China. Ground Water 38 (1), 38–45.

Yi, L., Dong, N., Zhang, L., Xiao, G., Wang, H., Jiang, X., 2019. Radium isotopes distribution and submarine groundwater discharge in the Bohai Sea. Groundwater Sustainable Dev. 9, 100242.

Younger, P.L., 1996. Submarine groundwater discharge. Nature 382 (6587), 121–122.

Zhang, X., Miao, J., Hu, B.X., Liu, H., Zhang, H., Ma, Z., 2017. Hydrogeochemical characterization and groundwater quality assessment in intruded coastal brine aquifers (Laizhou Bay, China). Environ. Sci. Pollut. Res. Int. 24 (26), 21073–21090.

Zamrsky, D., Karssenberg, M.E., Cohen, K.M., Bierkens, M.F., Oude Essink, G.H., 2020. Geological heterogeneity of coastal unconsolidated groundwater systems worldwide and its influence on offshore fresh groundwater occurrence. Front. Earth Sci. 339, 1–5. https://doi.org/10.3389/feart.2019.00339.

Zhou, Y., Sawyer, A.H., David, C.H., Famiglietti, J.S., 2018. Global estimates of submarine groundwater discharge reveal heightened threat of saltwater intrusion to mid-latitude aquifers, AGU Fall Meeting Abstracts. http://www.2018AGUFM.H11D..03Z.